

Measuring galaxy environment with the synergy of future photometric and spectroscopic surveys

O. Cucciati,^{1,2★} F. Marulli,^{1,2,3} A. Cimatti,² A. I. Merson,⁴ P. Norberg,⁵ L. Pozzetti,¹ C. M. Baugh⁵ and E. Branchini^{6,7,8}

¹INAF-Osservatorio Astronomico di Bologna, via Ranzani 1, I-40127 Bologna, Italy

²Dipartimento di Fisica e Astronomia - Università di Bologna, viale Bertini Pichat 6/2, I-40127 Bologna, Italy

³INFN, Sezione di Bologna, viale Bertini Pichat 6/2, I-40127 Bologna, Italy

⁴Department of Physics & Astronomy, University College London, London WC1E 6BT, UK

⁵ICC, Department of Physics, Durham University, South Road, Durham DH1 3LE, UK

⁶Dipartimento di Matematica e Fisica, Università degli Studi Roma Tre, via della Vasca Navale 84, I-00146 Roma, Italy

⁷INFN, Sezione di Roma Tre, via della Vasca Navale 84, I-00146 Roma, Italy

⁸INAF - Osservatorio Astronomico di Roma, via Frascati 33, I-00040 Monte Porzio Catone (RM), Italy

Accepted 2016 July 14. Received 2016 July 13; in original form 2016 March 31

ABSTRACT

We exploit the synergy between low-resolution spectroscopy and photometric redshifts to study environmental effects on galaxy evolution in slitless spectroscopic surveys from space. As a test case, we consider the future *Euclid* Deep survey (~ 40 deg²), which combines a slitless spectroscopic survey limited at $H\alpha$ flux $\geq 5 \times 10^{-17}$ erg cm⁻² s⁻¹ and a photometric survey limited in H band ($H \leq 26$). We use *Euclid*-like galaxy mock catalogues, in which we anchor the photometric redshifts to the 3D galaxy distribution of the available spectroscopic redshifts. We then estimate the local density contrast by counting objects in cylindrical cells with radius from 1 to 10 h^{-1} Mpc, over the redshift range $0.9 < z < 1.8$. We compare this density field with the one computed in a mock catalogue with the same depth as the *Euclid* Deep survey ($H = 26$) but without redshift measurement errors. We find that our method successfully separates high- from low-density environments (the last from the first quintile of the density distribution), with higher efficiency at low redshift and large cells: the fraction of low-density regions mistaken by high-density peaks is < 1 per cent for all scales and redshifts explored, but for scales of 1 h^{-1} Mpc for which is a few per cent. These results show that we can efficiently study environment in photometric samples if spectroscopic information is available for a smaller sample of objects that sparsely samples the same volume. We demonstrate that these studies are possible in the *Euclid* Deep survey, i.e. in a redshift range in which environmental effects are different from those observed in the local Universe, hence providing new constraints for galaxy evolution models.

Key words: surveys – large-scale structure of Universe.

1 INTRODUCTION

Environment is known to play a role in galaxy evolution, especially at relatively low redshift ($z \lesssim 1$) and for galaxies with small to intermediate stellar mass ($\log(M/M_{\odot}) \lesssim 10.5$; see e.g. Bolzonella et al. 2010; Davidzon et al. 2016). There are still many open debates on this subject, ranging from the relation between the 3D galaxy distribution and the underlying dark matter (DM) structures, to the actual physical processes that shape galaxy properties, which take place in different environments and on different time-scales. Only

through observations at different epochs, we can robustly derive a coherent picture of galaxy evolution.

Ideally, we need to probe from large to small scales, over a large span in redshift, and with large statistics, to allow us to robustly measure galaxy properties in different environments. Several physical processes that shape galaxy properties take place in galaxy groups and clusters (e.g. galaxy–galaxy merging, Toomre & Toomre 1972, ram pressure stripping of gas, Gunn & Gott 1972, strangulation, Larson, Tinsley & Caldwell 1980, harassment, Moore et al. 1996 and so on), so the study of local, high-density environment on small scales is crucial. Moreover, the cosmic web is continuously evolving with time, and each galaxy can live in very different environments during its lifetime. As a consequence, we need to be able to study

* E-mail: olga.cucciati@oabo.inaf.it.

how environment evolves to understand how it shapes galaxy evolution, and at the same time we need to study how the properties of the overall galaxy population change with time. For instance, it would be important to understand if and how we can link the peak of the star formation rate (SFR) density ($z = 1.5\text{--}2$, see e.g. Cucciati et al. 2012a and Madau & Dickinson 2014) with the onset of the relation between SFR and local density (Cucciati et al. 2006; Lin et al. 2016 at $z \gtrsim 1.2$, Elbaz et al. 2007 at $z \sim 1.1$, but see also Kodama et al. 2007; Spitler et al. 2012 for the identification of red massive galaxies in high-redshift clusters). Finally, we need large galaxy samples to remove the degeneracies among the many parameters that regulate the galaxy evolution processes (e.g. the complex interplay between local environment, stellar mass and star formation (SF), like for instance in Peng et al. 2010; McNaught-Roberts et al. 2014 and references therein).

In this framework, the ability of identifying and isolate a representative sample of high-density structures is of paramount importance. This would simultaneously require high accuracy in the redshift measurement, large galaxy density and large volumes. These requirements cannot be met by standard spectroscopic surveys performed with current instruments, since the required observation time would be prohibitively large. In addition, since we aim to trace galaxy evolution, we should target galaxies at relatively high redshift. To optimize the targeting of such galaxies using multi-object spectrographs, some kind of target pre-selection in near-IR bands is required, but ground-based observations in the near-IR are limited by the atmospheric transmission windows.

A photometric galaxy survey would provide us with large statistics and a large span in redshift within a much shorter time-scale of observations. Many studies in the literature make use of photometric redshifts to derive local environment. These analyses include galaxy cluster identification (e.g. Mazure et al. 2007; Adami et al. 2010; Bellagamba et al. 2011; Jian et al. 2014), detailed studies of extended structures (e.g. Cassata et al. 2007; Guzzo et al. 2007), and a broad analysis of the entire range of density enhancements, from empty regions to the highest density peaks (see e.g. Scoville et al. 2007, 2013; Darvish et al. 2015; Lin et al. 2016). The price to pay is the much lower (>1 dex) redshift precision with respect to spectroscopic redshifts, which hampers the precision of the 3D reconstruction of local environment on small scales (e.g. Cooper et al. 2005; Lai et al. 2016 and Malavasi et al. 2016).

Alternatively, one could carry out narrow-band photometric surveys, with filters aimed to target emission line galaxies (ELG) in a very narrow redshift bin (e.g. the HiZELS and NEWFIRM $H\alpha$ surveys, see Geach et al. 2008; Ly et al. 2011). The main drawbacks of this approach are the very limited redshift bin and the possible contamination from other emission lines.

Slitless spectroscopy of ELG is a compromise between redshift precision and being able to probe a large volume (both wide and deep) in a relative short exposure time. This kind of spectroscopy uses a prism or grism as dispersing element, so the spectral resolution can be very high. However, all the sources on the sky plane are spread out into their spectrum at once, and as a consequence the information on the angular position of the sources is limited and spectra can partially overlap. Spectra overlap might be significant especially in crowded fields, like deep samples, and in high-density regions, that are important targets of environmental studies. The impact of this contamination can be reduced to some extent by taking observations of the same field at different position angles.

If a survey based on slitless spectroscopy is carried out from space, the collected data do not suffer from atmospheric absorption. This is the case, for instance, of the slitless surveys performed with

the *Hubble Space Telescope* (HST), based on NICMOS (McCarthy et al. 1999; Yan et al. 1999; Shim et al. 2009) and on the WFC3. The WFC3 Infrared Spectroscopic Parallels programme (WISP; Atek et al. 2010, 2011) represents a major improvement with respect to the previous programme based on NICMOS, given that the WFC3 field of view is much larger than that of NICMOS. These HST observations will be followed, in the future, by slitless spectroscopic surveys from two other space missions, the European Space Agency's *Euclid* (Laureijs et al. 2011) and the National Aeronautics and Space Administration's WFIRST (Wide-Field Infrared Survey Telescope; Dressler et al. 2012; Green et al. 2012).

Space-based slitless spectroscopy of ELGs thus represents a potential new advancement in environmental studies, although it also suffers from some drawbacks. For instance, the deeper the observations, the greater number of spectra which will overlap on the image. At the same time, keeping the depth fixed, in overdense regions the sky is more crowded than in low-density regions, increasing the contamination from adjacent spectra. A way to tackle this problem is to repeat observations at the same position but with different position angles, but this comes at the expense of a longer total exposure time.

A promising way to study local environment on small scales over large volumes is through the synergy of photometric and spectroscopic galaxy samples. For instance, one can anchor the photometric redshifts to a robustly defined 3D skeleton, built with a (sub)sample of galaxies with spectroscopic redshifts. A density estimator based on such a method has been successfully developed for the zCOSMOS survey (Lilly et al. 2007) by Kovač et al. (2010). Cucciati et al. (2014) applied a simplified version of the same method to the VIPERS survey (Garilli et al. 2014; Guzzo et al. 2014).

The feasibility of such studies has to be evaluated case by case, according to the selection function of the planned surveys. For instance, the zCOSMOS and VIPERS samples are both flux-limited at $i = 22.5$, but the zCOSMOS spectroscopic sample has a higher target sampling rate, and the zCOSMOS ancillary photometric catalogue has a smaller photometric redshift error. For these two reasons, the analysis performed with the zCOSMOS sample is robust down to smaller scales than those reached with VIPERS. The higher sampling rate of the zCOSMOS survey comes at the price of a much smaller covered area, and only with a survey as large as VIPERS we can investigate the properties of rare objects with large statistical significance.

The future *Euclid* mission will provide the community with both slitless spectroscopic observations and photometric observations of a flux-limited sample of galaxies. The slitless spectroscopy will sample ELGs, while the photometric observation will be limited in H band. The improvements with respect to current ground-based spectroscopic surveys at $z \lesssim 1$ consist of larger and deeper photometric and spectroscopic catalogues, that might allow environmental studies up to $z \sim 2$ on relatively small scales.

Here, we use galaxy mock catalogues which mimic the *Euclid* Deep spectroscopic and photometric surveys to assess the possibility of studying how environment affects galaxy evolution at high redshift by exploiting the synergy between spectroscopic and photometric samples. The approach relies on the ability of sampling high-versus low-density regions rather than reconstructing the whole density field and its correlation properties as in the galaxy clustering studies. In this work, we shall therefore focus on the ability to discriminate high-density environments from the low-density ones.

This paper is organized as follows. In Section 2, we present the mock galaxy catalogues that we use in this work, and in Section 3 some of their properties, such as number counts and their clustering

strength. Section 4 describes how we estimate the density field using both the photometric and spectroscopic galaxy catalogues. Our results on the reliability of the environmental parametrization are detailed in Section 5, and we show a test case in Section 6. We summarize our results in Section 7.

We use a cosmology based on a Λ cold dark matter (Λ CDM) model with $\Omega_m = 0.272$, $\Omega_\Lambda = 0.728$, $H_0 = 70.4 \text{ km s}^{-1} \text{ Mpc}^{-1}$, i.e. the cosmology in which our mock galaxy catalogues are based. Magnitudes are in the AB system (Oke 1974).

2 A TEST CASE: THE *EUCLID* DEEP SURVEY

Several next-generation cosmological projects are conceived to comprise both a spectroscopic and a photometric survey, so to exploit two independent cosmological probes at once: the baryonic acoustic oscillations (BAO) and weak gravitational lensing (WL), respectively.

In this respect, such projects naturally provide the two data sets required for our strategy: a spectroscopic and a photometric sample. We will consider the *Euclid* mission as a realistic case to illustrate the potential of next-generation surveys in environmental studies.

2.1 The *Euclid* Deep survey

Full details on the *Euclid* mission surveys are given in the *Euclid* Definition Study Report (Laureijs et al. 2011, ‘Red Book’ from now on). The pieces of information most relevant for this work are the following.

The *Euclid* mission comprises a Wide and a Deep survey, each of them based on photometric and spectroscopic (slitless) observations. The Wide survey will cover a sky area of $15\,000 \text{ deg}^2$, with a flux limit of $H = 24$ (5σ point source) for the NIR photometry and an $H\alpha$ line flux limit of $\sim 3 \times 10^{-16} \text{ erg cm}^{-2} \text{ s}^{-1}$ (3.5σ unresolved line flux) for the spectroscopy. Thanks also to ancillary photometry from other surveys, it will be possible to compute photometric redshifts (z_p) for the sources in the photometric catalogue. The z_p measurement error is required to be at most $\sigma_{z_p} = 0.05(1+z)$, with a maximum 10 per cent of catastrophic measurement failures. The spectroscopic redshifts (z_s) of the spectroscopic survey are required to have a maximum measurement error of $\sigma_{z_s} = 0.001(1+z)$.

The Deep survey will be two magnitudes deeper than the wide one, but will cover a much smaller sky area ($\sim 40 \text{ deg}^2$). Namely, the photometric deep survey will be flux-limited at $H = 26$ (5σ point source) and the $H\alpha$ flux limit for the spectroscopic part will be $\sim 5 \times 10^{-17} \text{ erg cm}^{-2} \text{ s}^{-1}$ (3.5σ unresolved line flux). The required maximum values of photometric and spectroscopic redshift errors are the same as for the Wide survey.

The upper value for σ_{z_p} , i.e. $0.05(1+z)$, is granted by the use of the *Euclid* photometry in three NIR bands (Y, J, H) covering the wavelength range $0.92\text{--}2.0 \mu\text{m}$, and the use of at least four optical bands (from ground-based data, such as the ‘*griz*’ filter set) covering the range $420\text{--}930 \text{ nm}$. The depth of these observations needs to be at least 24 for the three NIR bands, and $g = 24.4$, $r = 24.1$, $i = 24.1$ and $z = 23.7$ in the optical. These requirements apply to the *Euclid* Wide survey. For the Deep survey, they need to be ~ 2 mag deeper. To keep σ_{z_p} as low as possible, it is also important that the photometry is uniform within a single field, and across several fields. The requirement is to reach a relative photometric accuracy of 1.5 per cent for all the galaxies in the survey.

According to the Red Book, the total wavelength range covered by the slitless spectroscopy is $1.1\text{--}2.0 \mu\text{m}$, and it will allow us the detection of the $H\alpha$ line over the redshift range $0.7 \lesssim z \lesssim 2.05$.

In this work, we focus our attention to the Deep survey in the redshift range $0.9 \leq z \leq 1.8$. Basically, the Deep survey is conceived to help with the calibration of the Wide survey, which will be used for one of the *Euclid* main cosmological probes. Clearly, the Deep survey will also provide the community with unprecedented data sets for ancillary science. We want to exploit the full potentiality of such data in the field of environmental studies, where it is important to probe small scales, best reached with deep samples.

2.2 Mock galaxy samples

For our analysis, we use mock galaxy catalogues that mimic the *Euclid* Deep spectroscopic and photometric surveys (their flux limit, their redshift measurement error etc). We will refer to these catalogues as DSmOCKS and DPmOCKS, respectively, and also as *Euclid*-like catalogues. To assess the robustness of our environment reconstruction, we also need a catalogue as densely populated as the photometric catalogue, but with no photometric redshift error. The density estimated in this catalogue will be our reference computation. We call these reference catalogues DREFmOCKS.

We use mock galaxy samples built with the semi-analytical model of galaxy formation and evolution described in Gonzalez-Perez et al. (2014). This model was applied to the DM halo merging trees derived from a revision of the Millennium Simulation (Springel et al. 2005) run with a cosmology consistent with the 7 yr results of the *Wilkinson Microwave Anisotropy Probe* (WMAP7; Komatsu et al. 2011). Namely, the adopted cosmological model is a Λ CDM model with $\Omega_m = 0.272$, $\Omega_b = 0.0455$, $h = 0.704$, $\Omega_\Lambda = 0.728$, $n = 0.967$, and $\sigma_8 = 0.810$. The Millennium Simulation contains $N = 2160^3$ particles of mass $8.6 \times 10^8 h^{-1} M_\odot$ within a comoving box of size $500 h^{-1} \text{ Mpc}$ on a side.

The construction of the *Euclid*-like lightcone are fully described in Merson et al. (2013). The lightcones are stored in the Virgo Consortium Database¹ (Lemson & Virgo Consortium 2006). These lightcones contain the galaxy properties we need for our study, i.e. the observed H -band magnitude and the $H\alpha$ flux. For each galaxy, two redshifts are provided: the cosmological redshift (z_{cos}) and a redshift that includes both the cosmological redshift and the peculiar velocity (z_{pec}). We are interested in the second one, because we perform our analysis in redshift space. Two *Euclid*-like lightcones were available at the time of our analysis: one characterized by a wide area, with $H\alpha$ and H -band limits matching those of the *Euclid* Wide survey, and a deeper one, complete down to $H\alpha$ line flux of $\sim 3 \times 10^{-18} \text{ erg cm}^{-2} \text{ s}^{-1}$ and $H = 27$ (meaning that it comprises all the galaxies which satisfy at least one of the two selection criteria), covering a smaller, circular region of $\sim 20 \text{ deg}^2$. Note that the $H\alpha$ line flux and the H -band limits are both deeper than the selection criteria of the *Euclid* Deep survey. In this work we considered the latter lightcone, that we divided into four square-shaped independent lightcones of $2 \times 2 \text{ deg}^2$, from which we extracted the mocks used in our analyses, as follows.

(i) Galaxy mock catalogues with a flux limit of $H = 26$, mimicking the magnitude limit of the *Euclid* Deep photometric survey. We consider them as our reference catalogues, and we call them DREFmOCKS. These catalogues represent the *Euclid* Deep photometric survey without photometric redshift error, and the density field estimated in these catalogues (in redshift space) sets the reference to assess the robustness of the density field reconstruction.

¹ <http://galaxy-catalogue.dur.ac.uk:8080/Millennium/>

Table 1. List of the galaxy mock catalogues used in this work, with their main properties: the limiting flux in H band or $H\alpha$ flux, the redshift error added to the peculiar velocities, and other specific properties. For more details see Section 2.2.

| Name | Sky area deg ² | H -band flux limit (mag) | $H\alpha$ flux limit (erg cm ⁻² s ⁻¹) | Redshift error | Other properties |
|------------|------------------------------|-------------------------------|---|--------------------------------------|--------------------------------------|
| DREFMOCKS | 2 × 2 | 26 | – | None | – |
| DPMOCKS | 2 × 2 | 26 | – | $\sigma = 0.05(1 + z_{\text{pec}})$ | 10 per cent of catastrophic failures |
| RAWDSMOCKS | 2 × 2 | – | 7×10^{-17} | $\sigma = 0.001(1 + z_{\text{pec}})$ | – |
| DSMOCKS | 2 × 2 | – | 7×10^{-17} | $\sigma = 0.001(1 + z_{\text{pec}})$ | C=P=98 per cent. Adjusted $n(z)$. |

(ii) Galaxy mock catalogues with a flux limit of $H = 26$, in which galaxies have photometric redshifts (z_p). Namely, we took the DREFMOCKS and we added to the redshift z_{pec} of each galaxy a random value extracted from a Gaussian with $\sigma = 0.05(1 + z_{\text{pec}})$. We also added 10 per cent of catastrophic redshift measurements, by assigning a random redshift to 10 per cent of the galaxies (although this is a simplistic approximation). From now on we call these mock catalogues DPMOCKS.

(iii) Galaxy mock catalogues with an $H\alpha$ flux limit of 7×10^{-17} erg cm⁻² s⁻¹, mimicking the 5σ flux limit of the *Euclid* Deep spectroscopic survey (more conservative than the 3.5σ described in Section 2.1, see below for the reason of this choice). Galaxies in this sample will have spectroscopic redshifts (z_s) with a typical measurement error of $\sigma = 0.001(1 + z)$. To mimic this uncertainty, we added to the redshift z_{pec} of each galaxy a random value extracted from a Gaussian with $\sigma = 0.001(1 + z_{\text{pec}})$. From now on, we call these mock catalogues RAWDSMOCKS.

(iv) Galaxy mock catalogues with $H\alpha$ flux limit as close as possible to 7×10^{-17} erg cm⁻² s⁻¹, but with redshift distribution $n(z)$ adjusted to be consistent with predictions. Specifically, we take the RAWDSMOCKS, and we modify their $n(z)$ to match the $n(z)$ predicted by Pozzetti et al. (2016, see Section 3.1). This procedure basically consists in adding in the RAWDSMOCKS also galaxies with $H\alpha$ flux below 7×10^{-17} erg cm⁻² s⁻¹, as described in details in Section 3.1. We call these mock catalogues DSMOCKS.

From now on, we will use the DREFMOCKS as reference catalogues, and the DPMOCKS and DSMOCKS as ‘*Euclid*-like’ mock galaxy catalogues. We note that we adopted a very simplistic approach to mimic the *Euclid* selection function in these catalogues. In particular, it is important to explain some of the choices we made in the modelization of our mock catalogues.

The *Euclid* photometric survey will be characterized by masked sky areas, variations of σ_{z_p} with galaxy luminosity, and so on, but we do not take them into account. A full characterization of the photometric redshift probability distribution function (PDF) for the *Euclid* survey is still under study within the *Euclid* Consortium, so we cannot mimic, in our mock catalogues, the full z_p PDF nor the redshift distribution of the catastrophic z_p errors. For this reason, we decided to use a very simplistic approach, assuming the PDF to be Gaussian and the catastrophic z_p errors to be 10 per cent at all redshifts. This way, we do not take the risk of mimicking a sophisticated z_p observing procedure that is not representative of the *Euclid* one.

The spectroscopic sample can be characterized by its purity and completeness. The completeness, C , is defined as the fraction of spectroscopic targets for which it is possible to measure a redshift. The purity, P , is defined as the fraction of real targets among all the measured redshifts (spurious features due to noise etc. might be erroneously considered real $H\alpha$ lines). The spectroscopic *Euclid* Deep survey is designed, among other goals, to help with the computation of C and P for the Wide survey, so its C and P are foreseen

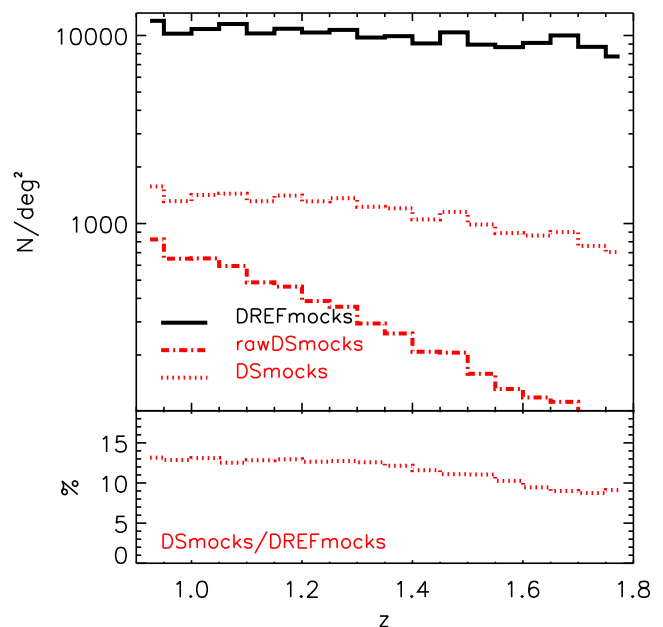


Figure 1. Top. Redshift distribution of the galaxies in the DREFMOCKS, RAWDSMOCKS and DSMOCKS, as detailed in the legend, in bins of $\Delta z = 0.05$. Bottom. Ratio of the redshift distribution of the DSMOCKS over the DREFMOCKS, expressed in percentage.

to be very close to 100 per cent at least for galaxies brighter than the *Euclid* Wide spectroscopic survey (3×10^{-16} erg cm⁻² s⁻¹). For galaxies with $H\alpha$ flux fainter than the Wide survey limit, C and P have not yet been computed, and they will possibly depend on redshift and $H\alpha$ flux.

For this reason, we decided to adopt, for our DSMOCKS, a $H\alpha$ flux limit of 7×10^{-17} erg cm⁻² s⁻¹, which corresponds to the flux limit of the Deep survey at $\sim 5\sigma$, instead of the nominal one at 3.5σ , and we consider the Deep survey to have $C=P=98$ per cent down to the $\sim 5\sigma$ flux limit. We mimicked C and P by removing 2 per cent of the galaxies (randomly chosen, irrespectively of their position or flux), and adding a corresponding number of fake objects (randomly placed in the survey volume).

We verified the robustness of the density field reconstruction in the case of a brighter $H\alpha$ flux limit for the DSMOCKS, to understand what would change in case our assumption of $C=P=98$ per cent down to 7×10^{-17} erg cm⁻² s⁻¹ is too optimistic. In Appendix B, we show the results on the density field reconstruction if we use DSMOCKS with $H\alpha$ flux $> 10^{-16}$ erg cm⁻² s⁻¹, and we show that a brighter limit would affect only marginally our results.

In Table 1, we summarize the main properties of the galaxy mock catalogues listed above. In Fig. 1, we show the redshift distribution $n(z)$ of our mock catalogues. The density of galaxies in the DSMOCKS ranges between $\lesssim 15$ and ~ 10 per cent of the density of galaxies

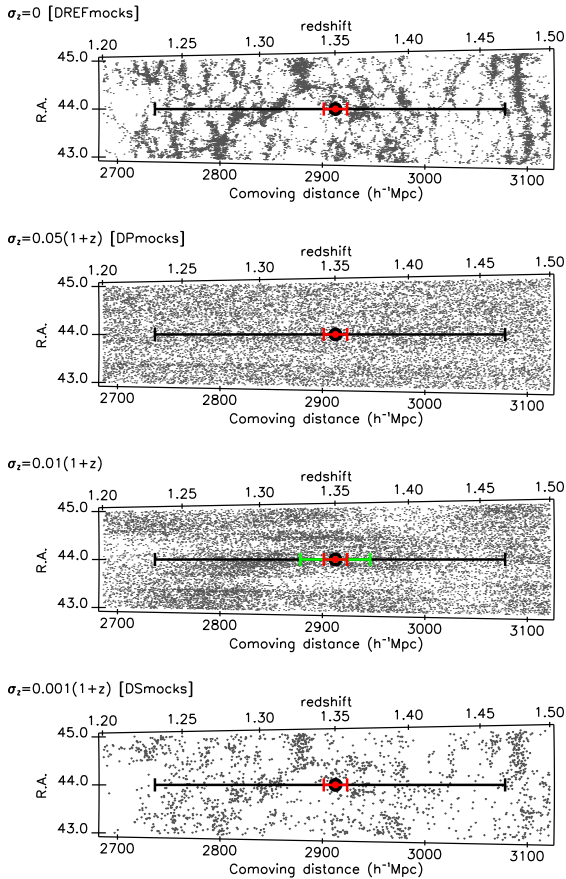


Figure 2. Example of RA– z distribution of galaxies in one of the lightcones used in this work, in the redshift range $1.2 < z < 1.5$. The projected *Dec* covers a range of $0:5$. Top: all galaxies in the DREFMOCK (flux limit at $H = 26$, 100 per cent sampling rate, the redshift includes cosmological redshift and peculiar velocity). Middle-top: galaxies in the DPMOCK obtained from the DREFMOCK in the top panel. Middle-bottom: only for reference, in this panel we show the galaxies in the DREFMOCK after adding a photometric redshift error of $\sigma = 0.01(1+z)$, i.e. five times less than the one we use in our DPMOCK. Bottom: galaxies in the DSMOCK extracted from the same lightcone as the DREFMOCK in the top panel. In all panels, the black horizontal line represents the photometric redshift error $\pm\sigma = 0.05(1+z)$ and the red line the spectroscopic redshift error $\pm\sigma = 0.001(1+z)$, both evaluated at $z = 1.35$. In the third panel, the green horizontal line represents a redshift error of $\pm\sigma = 0.01(1+z)$.

in the DPMOCKS, going from $z = 0.9$ to 1.8 . We note that, in the redshift range of interest ($0.9 < z < 1.8$), basically all the galaxies in the DSMOCKS also belong to the DPMOCKS.

Fig. 2 shows the RA– z distribution of galaxies in one of the lightcones used in this work, in the redshift range $1.2 < z < 1.5$. For the given lightcone, we show how galaxies are distributed in the DREFMOCK, DPMOCK, and DSMOCK. It is clear that the large photometric redshift error in the DPMOCK smears out the small- and large-scale structures visible in the DREFMOCK. For a comparison, in Fig. 2 we also show what would happen to the DREFMOCK when adding a photometric redshift error of $\sigma_{zp} = 0.01(1+z)$, that roughly corresponds to one of the smallest photometric redshift errors obtained with real data to date (see e.g. Ilbert et al. 2013, 2015 in the COSMOS field, who find $\sigma_{zp} = 0.008(1+z)$ for galaxies with $i < 22.5$). At $z \sim 1.3$ as in the figure, $\sigma_{zp} = 0.01(1+z)$ corresponds roughly to the scale of voids/underdense regions, as is evident from comparing the green line in the third panel with

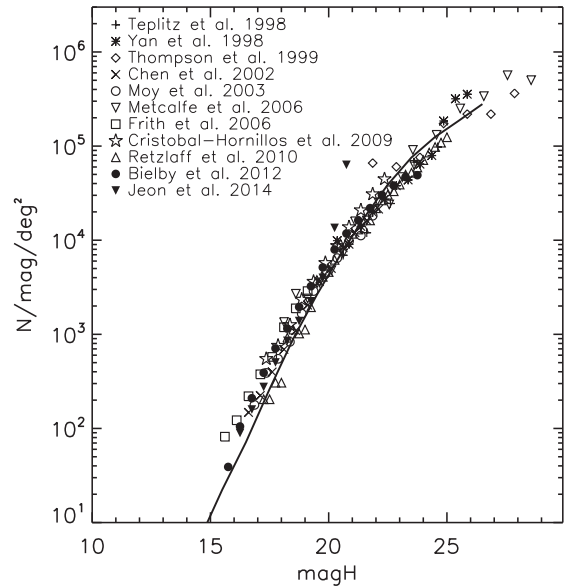


Figure 3. H -band number counts in our lightcones (black solid line) and in some observational data (symbols as in the legend).

the typical dimension of the empty areas in the top panel. This way, the galaxies in the most overdense structures do not mix too much when the photometric redshift error is added, and it is still possible to identify high-density regions (see also Malavasi et al. 2016).

3 PROPERTIES OF THE MOCK SAMPLES

In this section we study the number counts, the redshift distribution $n(z)$ and the clustering strength of the photometric and spectroscopic mock catalogues and we compare them with available data in the literature. This comparison is important, since the consistency between real and mock samples is a key to guarantee the reliability of our environmental study forecast.

3.1 Number counts and redshift distributions

Fig. 3 shows the H -band number counts ($N \text{ deg}^{-2} \text{ mag}^{-1}$) in our lightcones, compared with some observational data (Teplitz et al. 1998; Thompson et al. 1999; Yan et al. 1999; Chen et al. 2002; Moy et al. 2003; Frith, Metcalfe & Shanks 2006; Metcalfe et al. 2006; Cristóbal-Hornillos et al. 2009; Retzlaff et al. 2010; Bielby et al. 2012; Jeon et al. 2014). The counts in the mock catalogues are consistent with the observed galaxy counts in the range $19 \lesssim H \lesssim 23$. Below $H \sim 19$, predicted counts tend to underestimated the observed ones, up to a factor of $\lesssim 2$ at the brightest magnitudes, but this lack of objects is mainly related to galaxies at $z \lesssim 0.8$, a redshift range that is not studied in our work. The counts in the mock catalogues also seem to overestimate the observed counts at $H \gtrsim 23$ by a factor of ~ 50 per cent, but at these faint magnitudes the scatter in the real data is large. Overall, there is a fair agreement between the counts in the lightcones and in the real data.

The $H\alpha$ counts are not well constrained yet by observations, and yet the assessment of reliable forecasts of the $H\alpha$ number counts and redshift distribution is a crucial task for the preparation of the observational strategy for future missions like *Euclid* and WFIRST. We expect a large number of $H\alpha$ emitters in the redshift range explored by such missions, given that the cosmic SFR was higher in the past, with a peak at $z \sim 2$ (see e.g. Cucciati et al. 2012a; Madau

& Dickinson 2014). Moreover, the use of star-forming galaxies to study the small-scale environment at high redshift, like in our case, could be particularly effective if it is true (though the debate is still open in the literature) that SF galaxies reside preferentially in high densities at $z \gtrsim 1-1.5$ (Cucciati et al. 2006; Elbaz et al. 2007; Lin et al. 2016).

Several $H\alpha$ samples have been collected in the past years, using ground-based spectroscopy, grism spectroscopy from space and narrow-band NIR photometry. We refer the reader to Pozzetti et al. (2016) for the most recent compilation of such samples. Namely, Pozzetti et al. (2016) used these samples to derive three models of the evolution of the $H\alpha$ luminosity function (LF), to compute the forecasts for future surveys (see also Geach et al. 2010 for a previous modelization). We adopt ‘Model 1’ of Pozzetti et al. (2016) as the reference model in our analysis, because it includes the evolution of both L^* and ϕ^* , while ϕ^* does not evolve in their ‘Model 2’, and their ‘Model 3’ is based on a shorter redshift range.

We have compared the $n(z)$ of the galaxies in the RAWDSMOCKS (n_{mock}) with the predicted $H\alpha$ $n(z)$ of ‘Model 1’ (n_{mod}). The RAWDSMOCKS underestimate the predicted $n(z)$ at all redshifts (for the same flux limit, i.e. 7×10^{-17} erg cm $^{-2}$ s $^{-1}$), by an increasing factor going from $z = 0.9$ to 1.8. The RAWDSMOCKS contain 50 per cent (at $z = 0.9$) to 20 per cent (at $z = 1.8$) of the galaxies predicted by Pozzetti’s Model 1 (see their fig. 6). This is true for all $H\alpha$ fluxes above the *Euclid* flux limit (see their figs 4 and 5). We remark that the *Euclid* $H\alpha$ flux limit, even for the Deep survey, corresponds to values very close to L^* at $z \sim 1.5$, so the underestimate of $H\alpha$ counts in the mock catalogues is not (only) due to a possibly not well-constrained faint-end slope of the observed $H\alpha$ LF (see fig. 2 of Pozzetti et al. 2016 for the typical uncertainty of α in the literature).

To reproduce the predicted $H\alpha$ $n(z)$, we added galaxies in the RAWDSMOCKS until $n_{\text{mock}}(z)$ and $n_{\text{mod}}(z)$ were the same. Specifically, we picked up these new galaxies from the lightcones from which the RAWDSMOCKS were extracted, choosing randomly in RA–Dec. among the galaxies with $H\alpha$ slightly fainter than the flux limit of the RAWDSMOCKS. For each redshift bin z_i , we added fainter and fainter galaxies until $n_{\text{mock}}(z_i)$ matched $n_{\text{mod}}(z_i)$. At the end of the procedure, we had to add galaxies as faint as 2.5×10^{-17} erg cm $^{-2}$ s $^{-1}$ at $z \sim 1.0$, and even fainter galaxies at higher redshifts, down to 1.5×10^{-17} erg cm $^{-2}$ s $^{-1}$ at $z = 1.8$.

Following this procedure, we built the DSMOCKS from the RAWDSMOCKS. These modified mock catalogues are those called DSMOCKS in Section 2.2, in which we subsequently modelled the foreseen purity and completeness of the *Euclid* Deep spectroscopic survey, as described in Section 2.2. We show the redshift distribution of the RAWDSMOCKS and DSMOCKS in Fig. 1.

3.2 Two-point correlation function

Fig. 4 shows the galaxy two-point correlation function (2PCF) in the DREFMOCKS and DSMOCKS. We use DREFMOCKS instead of DPMOCKS for this exercise because our aim is to show the (possibly) different clustering strength for two samples selected in different ways (H band or $H\alpha$ flux) rather than to show how photometric redshift errors would affect the 2PCF (we expect that the small spectroscopic redshift error does not alter significantly the 2PCF in the DSMOCKS).

The 2PCF has been computed using the CosmoBolognaLib presented in Marulli, Veropalumbo & Moresco (2016). The random samples used to compute the 2PCF have been built adopting the

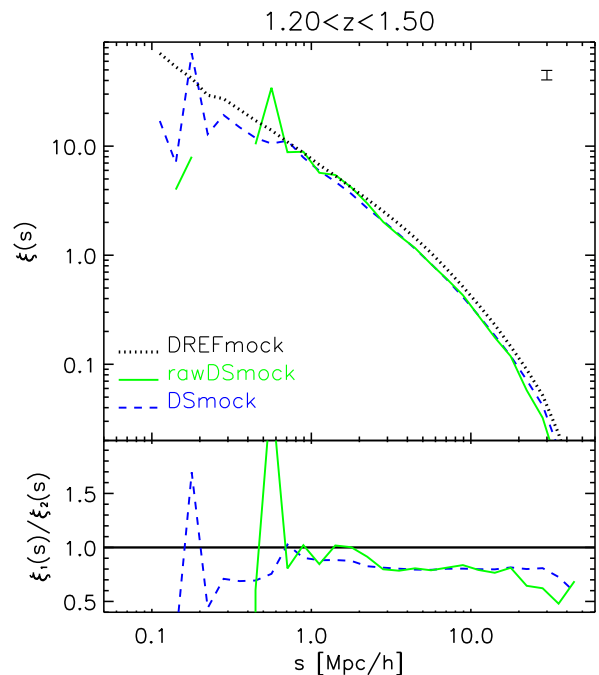


Figure 4. Top. Redshift–space galaxy 2PCF in different mock catalogues, in the redshift bin $1.2 < z < 1.5$. Different colours and styles are for different mock catalogues: the black dotted line is for DREFMOCKS, the green solid line for the RAWDSMOCKS, and the dashed blue line for DSMOCKS. The error bar in the top-right corner shows a difference in $\xi(s)$ of ± 10 per cent. Bottom. Ratio ξ_1/ξ_2 between the redshift–space galaxy 2PCF in the different mock catalogues shown in the top panel. The denominator (ξ_2) is always for DREFMOCKS, and the numerator are the RAWDSMOCKS and DSMOCKS catalogues (colour-code as in the top panel).

same geometrical selection of the DPMOCKS and DSMOCKS, and their specific $n(z)$. The figure shows that the galaxies in the photometric catalogue are more clustered than those in the spectroscopic sample, by a factor of ~ 20 per cent. This seems more evident for scales $r < 1 h^{-1}$ Mpc. We note that the two samples are not necessarily expected to have the same clustering (see e.g. the different clustering of galaxy populations with different stellar mass or luminosity, like in Li et al. 2006; Coil et al. 2008; Meneux et al. 2008; Christodoulou et al. 2012; Marulli et al. 2013).

Geach et al. (2012) measured the 2PCF of $H\alpha$ emitters in the Hi-Z Emission Line Survey (HiZELS) at $z \sim 2.2$. The HiZELS sample is complete down to 5×10^{-17} erg cm $^{-2}$ s $^{-1}$, that corresponds to $L_{H\alpha} > 10^{42}$ erg cm $^{-2}$ s $^{-1}$ at $z = 2.2$. They compared their results with the 2PCF of a galaxy sample extracted from the lightcones described in Merson et al. (2013). The lightcones were built with the semi-analytical model of galaxy formation and evolution described in Lagos et al. (2012), embedded in the DM halo merging trees derived from the Millennium Simulation (Springel et al. 2005). The sample extracted from the lightcones had the same selection function as the HiZELS sample. Geach et al. (2012) find that the mock galaxy sample based on the semi-analytical model, at the same redshift and $L_{H\alpha}$ as HiZELS, has less clustering than the HiZELS sample on scales $r < 0.5 h^{-1}$ Mpc, while the two samples have very similar clustering strength at larger scales.

We measured the 2PCF in the mock galaxy samples based on the semi-analytical model of Lagos et al. (2012), as in Geach et al. (2012), but in the same redshift ranges and for the same $H\alpha$ flux limit as in our DSMOCKS. We verified that their 2PCF is very similar to the one in our DSMOCKS, that are based on

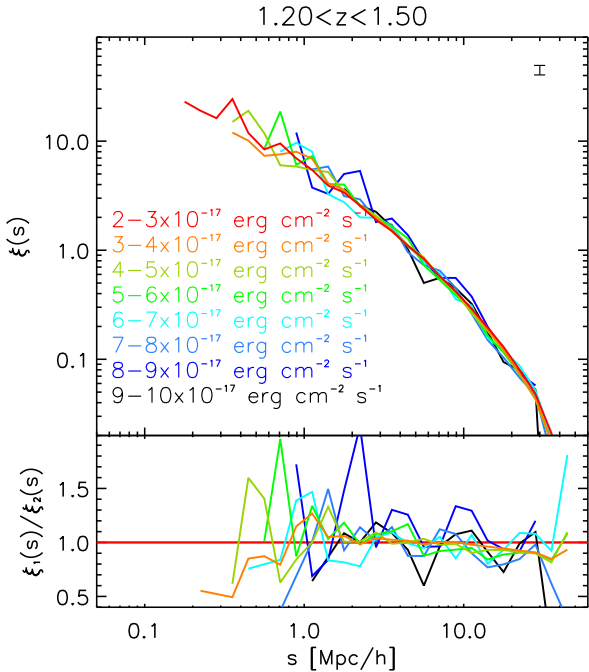


Figure 5. Top. Redshift–space galaxy 2PCF in the adopted lightcones (before applying any cut in H band or $H\alpha$) for different bins of $H\alpha$ flux down to $2 \times 10^{-17} \text{ erg cm}^{-2} \text{ s}^{-1}$, as in the labels, in the redshift bin $1.2 < z < 1.5$. Different colours are for different $H\alpha$ flux bins. The error bar in the top-right corner shows a difference in $\xi(s)$ of ± 10 per cent. Bottom. Ratio ξ_1/ξ_2 between the redshift–space galaxy 2PCF in the different mock catalogues shown in the top panel. The denominator (ξ_2) is always the 2PCF in the faintest flux bin ($\sim 2-3 \times 10^{-17} \text{ erg cm}^{-2} \text{ s}^{-1}$), and the numerator is for the other flux bins in the top panel (colour-code as in the top panel).

the semi-analytical model by Gonzalez-Perez et al. (2014). Even if the redshift explored in Geach et al. (2012) is slightly higher than our maximum redshift ($z = 1.8$), their results suggest that the small-scale clustering in our DSMOCKS is too weak with respect to real data.

We remark that the clustering properties of the spectroscopic sample are relevant for the method we use to estimate the density (see the discussion in Section 4.1 and Appendix A). We verified that the 2PCF of the fainter galaxies that we added in the RAWDSMOCKS to match the predicted $n(z)$ is not too different from the 2PCF of the galaxies with $H\alpha$ flux $> 7 \times 10^{-17} \text{ erg cm}^{-2} \text{ s}^{-1}$. This is shown in Fig. 4, where we also show the 2PCF for the RAWDSMOCKS , and in Fig. 5, where we show the 2PCF for different bins of $H\alpha$ flux, including fluxes below $7 \times 10^{-17} \text{ erg cm}^{-2} \text{ s}^{-1}$. This implies that adding fainter galaxies to reach the expected number counts does not alter the clustering strength of the galaxies with brighter $H\alpha$ flux.

4 LOCAL DENSITY AND ENVIRONMENT

The key quantity that we use to quantify environmental dependences is the local density contrast of galaxies, δ_N :

$$\delta_N = N/\langle N \rangle - 1, \quad (1)$$

where N is the number of objects in the volume element, and $\langle N \rangle$ the mean number of objects at a given redshift. Although δ is defined as a ‘density contrast’, we will often use simply

‘density’, for the sake of simplicity,² and we consider it as a proxy of environment.

We count objects in cylindrical cells of different sizes, all with the same half-length of 1000 km s^{-1} but different radii $R = 1, 2, 3, 5, 8, 10 h^{-1} \text{ Mpc}$ ($R_1, R_2, R_3, R_5, R_8, R_{10}$ from now on). The lengths of the radii are chosen to span from small scales (like clusters) to relatively large scales. Counts are performed by randomly throwing cells to oversample the survey volume. A cylindrical shape of the cells allows us to adopt a symmetric shape on the sky and an independent size along the line of sight, chosen to take into account the peculiar velocities of cluster galaxies.

We only consider cells fully contained within the survey area, which do not require any statistical correction for edge-induced incompleteness. We will consider the problems related to boundaries and gaps in the sky coverage in future work. We refer the reader to e.g. Cucciati et al. (2006) for an effective method for boundary correction in recent spectroscopic surveys, and to Cucciati et al. (2014) for some examples of gap-filling methods.

We call ‘tracer galaxies’ (or simply ‘tracers’) the galaxies used to estimate the local density. The choice of a given tracer sample is a compromise between the maximization of the number density (the denser the sample, the smaller the scales that can be reached in the density reconstruction) and the homogeneity of the sample across the surveyed area and along the explored redshift range.

Both the spectroscopic and the photometric *Euclid* surveys are flux-limited. As a consequence, the mean number density of objects decreases with redshifts. This is a rather typical situation that, however, does have an impact in environmental studies since it systematically modifies the minimum scalelength that we can effectively probe. One commonly adopted solution is to extract a subvolume limited catalogue of objects, for instance a luminosity-limited galaxy sample (see e.g. Cucciati et al. 2010; McNaught-Roberts et al. 2014). This has the advantage of providing a homogeneous sample of tracers with the same mean separation at all redshifts. The drawback is to throw away information at low redshifts (for instance, many faint galaxies will not be used as tracers), hampering our ability to probe small scales.

In this work, we want to assess the full potential of the data set at each redshift to investigate environmental effects, so we consider the whole flux-limited sample. For this reason, we expect that we will be able to better reconstruct the local density field on small scales at lower redshift.

Our aim is to reconstruct the density field in the *Euclid* photometric survey, minimizing the effects of the large photometric redshift error. For this we exploit the synergy of the photometric and spectroscopic *Euclid* surveys. The first one enjoys a large density of tracers with a large redshift measurement error, the second one is sparser, but the redshift measurement is much more precise. To assess how well we can reconstruct environment, we estimate the density contrast δ_N in three different mock galaxy catalogues:

(i) counts performed in the DREFMOCKS , by counting the galaxies falling within each cylindrical cell; we remind that in the DREFMOCKS , galaxy redshifts include peculiar velocities; we call this density contrast δ_N^R ;

(ii) counts performed in the DPMOCKS , by counting the galaxies falling within each cylindrical cell; we call this density contrast

² For the purposes of this paper, the density contrast δ is simply the way we define the environment, we do not need to physically distinguish it from the local density.

δ_N^p ; when compared with δ_N^R , it provides us with an estimate of the information lost due to the large photometric redshift errors;

(iii) counts performed in the merged *Euclid*-like $\text{DPMOCKS}+\text{DSMOCKS}$, in which the spatial distribution of the spectroscopic galaxies is exploited to improve the accuracy of the photometric redshift estimate (with the ZADE method, see the next section); we call the resulting density contrast δ_N^E .

4.1 The ZADE method

We use the so called ZADE method to modify the z_p PDF of the galaxies in the DPMOCKS exploiting the 3D distribution of the galaxies in the DSMOCKS . The ZADE method was developed for the zCOSMOS survey (Lilly et al. 2007), and is fully described in Kovač et al. (2010). We use a simplified version of the ZADE approach, that has already been tested for the VIPERS survey (Guzzo et al. 2014) by Cucciati et al. (2014).

In brief, this simplified ZADE method can be broken down into the following steps.

(i) For each galaxy in the DPMOCKS , we keep its angular position (RA and Dec.), and set the PDF of its photometric redshift ($P(z_p)$) to be equal to a normalized Gaussian centred on z_p and with standard deviation equal to the 1σ error in the photometric redshift, $\sigma_{z_p}=0.05(1+z)$.

(ii) We compute the spectroscopic redshift distribution $n(z_s)$ of the galaxies in the corresponding DSMOCK that fall within a cylinder centred on the position of the given photometric galaxy (RA, Dec., z_p), with radius R_{ZADE} (see below) and half-length equal to $3\sigma_{z_p}$.

(iii) We set a new PDF_{ZADE} for each galaxy in the DPMOCKS equal to $AP(z_p)n(z_s)$, where A is a factor to normalize the integral of PDF_{ZADE} to unity. PDF_{ZADE} is characterized by several peaks. The value of PDF_{ZADE} at each redshift peak corresponds to the weight w_{ZADE} at that given redshift, and for each photometric galaxy the sum of all its w_{ZADE} is unity by definition.

We note that the $n(z_s)$ is quite discontinuous (because of the limited number of spectroscopic galaxies) and, for this reason, we sample it in discretized bins of $\Delta z = 0.003$. For consistency, we sample the Gaussian $P(z_p)$ on the same grid. This way, PDF_{ZADE} has the form of a histogram, and we call ‘peaks’ all its bins where it is different from zero. Basically ZADE transforms a single photometric galaxy into a series of points at the same RA–Dec. position, and spread along the line of sight, with each point having a weight given by w_{ZADE} . For the estimation of the density field, the counts in the cylinders are computed summing up the weights w_{ZADE} of all the peaks that fall in the given cylinder.

The ZADE approach is particularly suitable to reconstruct the 3D galaxy distribution if the clustering properties of the spectroscopic sample used to compute the $n(z_s)$ are the same as the ones in the photometric sample (see e.g. the zCOSMOS and VIPERS surveys, where the spectroscopic data set was a random subset of the photometric one). In the case of *Euclid*, the photometric and spectroscopic surveys have different selections (limit in H band and in H α flux, respectively), so we cannot expect the two samples to have the same clustering, as discussed in Section 3.2.

Nevertheless, in the next sections we demonstrate that the ZADE method is very effective also in the case of the *Euclid* Deep survey, with respect of using photometric redshifts alone. We refer the reader to Appendix A for an example of how ZADE would work if we use, at the place of the DSMOCKS , a random subsample of the DPMOCKS (but with spectroscopic redshifts at the place of photometric ones).

We conclude with a remark on R_{ZADE} . The dimension of R_{ZADE} is chosen as a compromise between the need to minimize the probed scalelength (to use the clustering strength on small scales) and to maximize the number of spectroscopic galaxies in the cylinders (to reduce shot noise). We use $R_{\text{ZADE}} = 5 h^{-1}\text{Mpc}$, but we have checked the robustness of our density field reconstruction also by varying R_{ZADE} between 3 and 10 $h^{-1}\text{Mpc}$.

5 GAUGING THE ACCURACY OF THE DENSITY FIELD RECONSTRUCTION

In this section, we assess the ability of our method to trace the underlying galaxy density. First, we aim at separating low- from high-density environments to perform comparative studies of galaxy evolution (Sections 5.1 and 5.2). Then we move to the more challenging task of recovering the local galaxy density at a given position (Section 5.3). We discuss our results in the framework of environmental studies in Section 5.4.

More specifically, here we compare the density field δ_N^E obtained using the ZADE method in the $\text{DPMOCKS}+\text{DSMOCKS}$ to the density field estimated in the reference mock catalogues δ_N^R . As an additional check, we show also the comparison between δ_N^E and the density δ_N^p estimated in the DPMOCKS . The definition of δ_N is the one given in equation (1).

5.1 High- versus low-density regions

To test how well we can separate high- from low-density regions, we do not need to compare δ_N^E and δ_N^R on a point-by-point basis (as we will do in Section 5.3), but only their ranking.

For this purpose, we computed the PDF of δ_N^E and δ_N^R for the cell counts and sampled these PDFs in bins containing 10 per cent of the counts. We then computed the joint probability of δ_N^E and δ_N^R $P(\delta_N^E, \delta_N^R)$ using the same binning. This function is shown in Fig. 6, where, by construction, $P(\delta_N^E, \delta_N^R) = \int P(\delta_N^E, \delta_N^R) \delta_N^R d\delta_N^R = 10$ per cent = $P(\delta_N^E | \delta_N^R)$. The colour-coded probability value is such that in the generic δ_N^E (δ_N^R) bin the sum of the probability for δ_N^R (δ_N^E) is precisely 10 per cent. For a perfect reconstruction, the joint probability function would be everywhere equal to zero but for $\delta_N^R = \delta_N^E$, i.e. along the dotted line in the plot.

From the plots in Fig. 6 we see that

(i) the correlation between the ranked δ_N^R values and the ranked δ_N^E values is stronger (both in terms of a smaller deviation from the 1:1 correlation and a lower dispersion) for larger radii.

(ii) For R_1 , at low density the values of δ_N^R are discretized: the radius of the cylinder is very small with respect to the mean intergalaxy separation of the sample, so in many cylinders we have 0, 1 or 2 galaxies. This is apparent in Fig. 6, where δ_N^R is always binned in bins of 10 per cent. For R_1 , at low density, we have the first bin as large as ~ 20 per cent. This is the percentage range where $\delta_N^R = 0$. This does not happen for δ_N^E , because the ZADE method produces objects with fractional weights, so their counts result in a continuous δ_N^E distribution.

(iii) We also explored the redshift dependence of the correlation between δ_N^R and δ_N^E (see Appendix C), and we found that the above-mentioned results hold at all explored redshifts. Moreover, in general, at fixed radius the correlation is stronger for lower redshift, and this is especially true for small radii. This happens because at low redshift the mean galaxy density is higher (the galaxy sample is flux-limited), so the local density reconstruction suffers from a lower shot noise. Clearly this effect is more important for small radii,

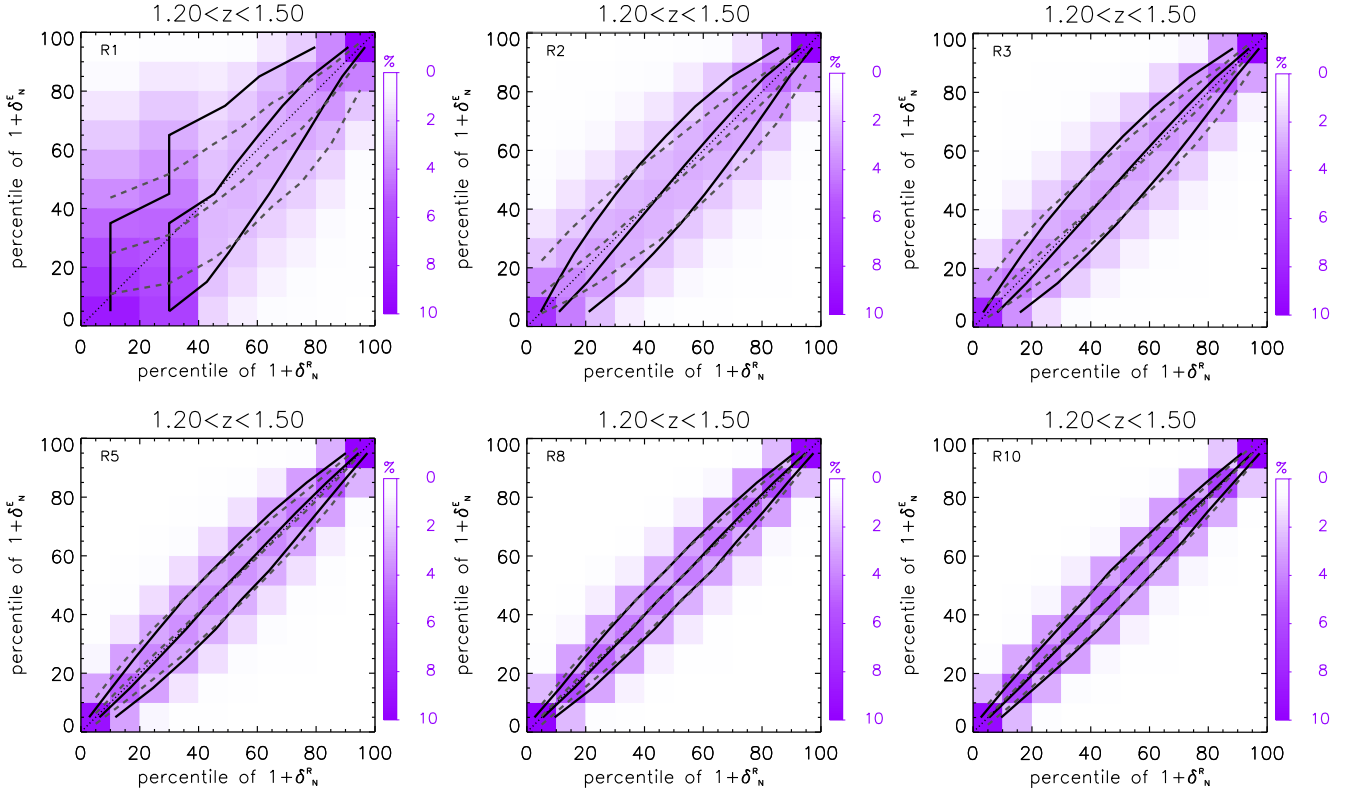


Figure 6. Joint probability distribution of $1 + \delta_N^R$ (x-axis) and $1 + \delta_N^E$ (y-axis), in equipopulated bins containing 10 per cent of the density measurements. $1 + \delta_N^R$ and $1 + \delta_N^E$ on the two axes are ranked in increasing order. The colour-coded probability value is such that in the generic δ_N^E (δ_N^R) bin the sum of the probability for δ_N^R (δ_N^E) is precisely 10 per cent, so the background colour code ranges from 0 per cent probability (white) to 10 per cent probability (dark violet) as indicated on the vertical bar on the right. The dotted line is the one-to-one line, for reference. Black solid lines show, for each bin of the y-axis, the 25th, 50th and 75th percentile of the distribution of $1 + \delta_N^R$ values. Grey dashed lines show, for each bin of the x-axis, the 25th, 50th and 75th percentile of the distribution of $1 + \delta_N^E$ values. For a perfect reconstruction, the joint probability function would be everywhere equal to zero but for $\delta_N^R = \delta_N^E$, i.e. along the dotted line in the plot. From top-left to bottom-right, the panels refer to different radii (R_1 , R_2 , R_3 , R_5 , R_8 and R_{10}); all panels refer to the redshift range $1.2 < z < 1.5$ (see Figs C1 and C2 for other redshift bins).

where the average counts-in-cells are lower and, as a consequence, their relative variation from low to high redshift is larger.

We notice that the scatter around the 1:1 correlation in Fig. 6, for the lowest³ and highest densities, is artificially low, simply because of the finite range of the density values.

To appreciate more the goodness of the density reconstruction based on both spectroscopic and photometric redshifts, in Fig. 7 we show the same as in Fig. 6 but this time we compare δ_N^R with the density reconstructed using only photometric redshifts (δ_N^P). The almost uniform colour of Fig. 7 shows that the large photometric errors erase any correlation between the rankings, making it impossible to separate high- from low-density environments using only a photometric survey with a photometric redshift error of $\sigma_{zp} = 0.05(1+z)$.

5.2 Completeness and contamination

Fig. 6 shows which is the range of δ_N^R that corresponds to any given selection on δ_N^E . For a more quantitative analysis, we can choose some specific δ_N^E ranges and compute their completeness and contamination, as follows.

³ For all radii but R_1 , because of the discretized density values discussed in the text.

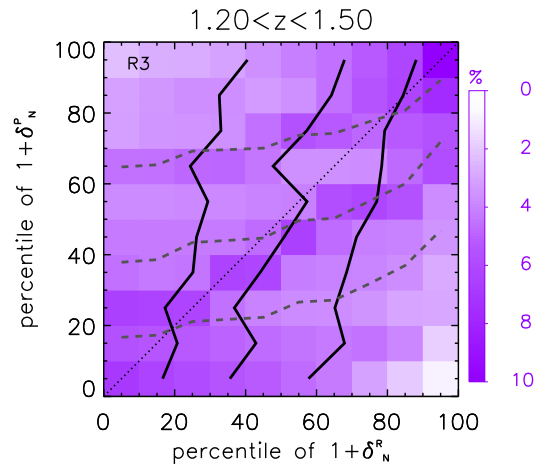


Figure 7. As in Fig. 6, but in this case the y-axis shows $1 + \delta_N^P$. The panel refers to R_3 over the redshift range $1.2 < z < 1.5$. For a perfect reconstruction, the joint probability function would be everywhere equal to zero but for $\delta_N^R = \delta_N^P$, i.e. along the dotted line in the plot.

For each cylinder radius and redshift, we call N_i^E (N_i^R) the number of cylinders falling in the percentile range i of the δ_N^E (δ_N^R) distribution. Also, we call $N_{i,j}^{E,R}$ the number of cylinders that fall in the percentile range i of δ_N^E and in the percentile j of δ_N^R . We then

select a given percentile range i and define its completeness and contamination as

$$\text{completeness} = N_{i,i}^{E,R} / N_i^R \quad (2)$$

$$\text{contamination} = N_{i,j}^{E,R} / N_i^E \quad (\text{with } i \neq j). \quad (3)$$

Namely, the completeness indicates the fraction of cylinders that are placed in the correct percentile. The contamination shows which fraction of cylinders belonging to the percentile i of δ_N^E distribution come from a different percentile of the original δ_N^R distribution. Ideally one would like a completeness of 100 per cent and a contamination equal to zero.

Fig. 8 shows the completeness and the contamination for our *Euclid*-like mock catalogues. We analyse three percentile ranges (i) of the δ_N^E distribution: $80^{\text{th}}-100^{\text{th}}$, $40^{\text{th}}-60^{\text{th}}$, and $0^{\text{th}}-20^{\text{th}}$. Basically, they correspond to the highest, intermediate and lowest density regimes, that we call P_H , P_I , and P_L , respectively. For P_H and P_L , we show the completeness and the contamination coming from the other density regimes.

We find that:

(i) for all the density regimes, the completeness (/contamination) increases (/decreases) for lower redshift and for larger radii; the dependence of the completeness on redshift is especially evident at small radii for P_L ; in all cases, the completeness varies more with radius (at fixed redshift) than with redshift (at fixed radius);

(ii) at fixed radius and redshift, P_H is the most complete, having always a completeness $\gtrsim 60$ per cent at all radii and redshifts; this is due to the smaller random error in the density reconstruction (see Fig. 9) for the highest densities; this difference is especially true at small radii, where the reconstruction of the low densities is more difficult;

(iii) the contamination of P_L and P_H from the opposite density regime (P_H and P_L , respectively) is very low, being always below 1 per cent but for R_1 for which it gets to a few per cent; this implies that we can always safely separate P_L from P_H ;

(iv) for R_8 and R_{10} at all redshifts, and for R_5 at the lowest redshift, the contamination in P_H and P_L coming from P_I is below 2 per cent; this implies that for these radii and redshift ranges it is possible to study environment in three different density regimes, instead of selecting only P_L and P_H ;

(v) for R_5 , R_8 and R_{10} the completeness in P_H and P_L is very similar (always $\gtrsim 75$ per cent), as can be derived by the similar behaviour at the lowest and highest densities in Fig. 6; for smaller radii, we still have a good completeness for P_H ($\gtrsim 55$ per cent, $\gtrsim 60$ per cent, and $\gtrsim 70$ per cent for R_1 , R_2 and R_3 , respectively).

A caveat about the contamination from P_L : for R_1 the values of δ_N^R at the lowest densities are discretized (see Section 5.1), and in the three redshift bins the lowest δ_N^R value is taken by 20, 20 and 30 per cent of the cylinders (from low to high redshift). This means that the points at $1.5 < z < 1.8$ for R_1 in the top panel of Fig. 8 represents a contamination from the percentile range 0–30 per cent instead of from the range 0–20 per cent as all the other points in the figure.

In summary, we have shown that we can robustly identify high-density regions and distinguish them from the lowest densities, at all explored scales and at all explored redshift. The level of completeness of the selected sample of high-density regions depends on the scale and on the redshift, but the contamination from the lowest densities is always below a few per cent for R_1 and < 1 per cent for larger radii. We identify high densities in a more complete way

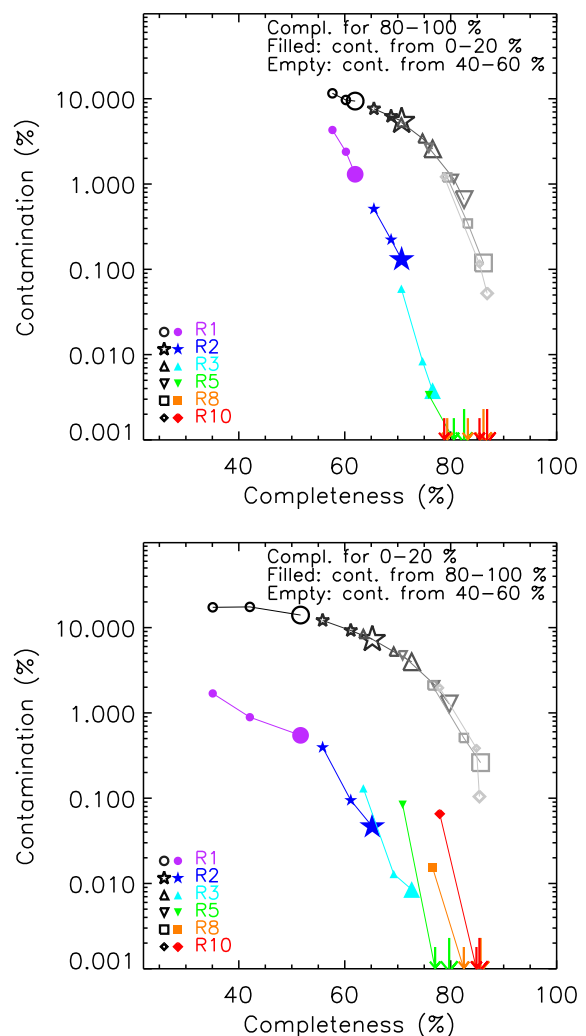


Figure 8. Completeness (x -axis) and contamination (y -axis) for our density reconstruction (see section 5.2 for the definition of completeness and contamination). Contamination and completeness are shown for all cylinder radii (different symbols as in the legend), and for three redshift bins ($0.9 < z < 1.2$, $1.2 < z < 1.5$, $1.5 < z < 1.8$). The three redshift bins for each radius are connected with a line, with the lowest redshift bin indicated with a bigger symbol. For each radius there are two series of points (filled coloured and empty grey shades) that refer to contamination coming from two different percentile ranges, as indicated in the panels. Top. Completeness for the tail of the highest $80^{\text{th}}-100^{\text{th}}$ percentiles and contamination from the $0^{\text{th}}-20^{\text{th}}$ percentiles (filled symbols) and from the $40^{\text{th}}-60^{\text{th}}$ percentile (empty symbols). Bottom. As the top panel, but the completeness is computed for the lowest densities (0–20 per cent), and its contamination comes from the $40^{\text{th}}-60^{\text{th}}$ percentile range (empty symbols) and from the $80^{\text{th}}-100^{\text{th}}$ percentile range (filled symbols). See the text for a caveat on the points for R_1 at $1.5 < z < 1.8$ in the top panel.

than low densities, especially at small scales. Moreover, for $R \geq 5 h^{-1} \text{Mpc}$ we can separate very well high densities also from intermediate densities (the contamination is only by a few per cent).

5.3 Density–density comparison

In this section we move to a more demanding test, i.e. we compare the values of δ_N^E and δ_N^R on a cell-by-cell basis. The aim of this density–density comparison is to estimate the systematic deviation from the true value and the random dispersion around the mean

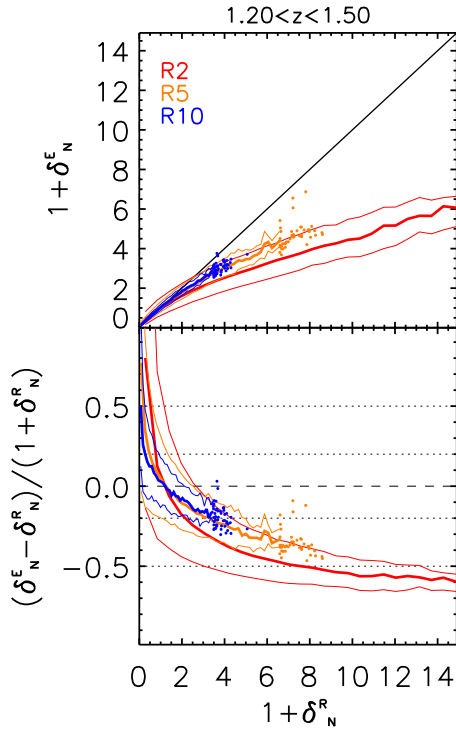


Figure 9. Comparison of δ_N^R and δ_N^E on a cell-by-cell basis. *x*-axis: density contrast in the reference catalogue ($1 + \delta_N^R$); *y*-axis, top panel: density contrast in the *Euclid*-like catalogue ($1 + \delta_N^E$); *y*-axis, bottom panel: relative difference ($(\delta_N^E - \delta_N^R)/(1 + \delta_N^R)$). The thick lines are the median value of the quantity displayed on the *y*-axis in each *x*-axis bin. Thin lines represent the 16th and 84th percentiles of its distribution. Points are single cells, when cells per bin are < 20 (in which case we do not compute a median and percentiles). The solid black line in the top panels is the one-to-one line, and the horizontal lines in the bottom panels are for reference. Results are shown for different cylinder radii as in the label (R_2 , R_5 and R_{10}) for the redshift bin $1.2 < z < 1.5$. See Fig. C3 for other redshift bins.

value for the single cells, to quantify the goodness of the density reconstruction at a local level.

In Fig. 9, we compare δ_N^R with δ_N^E , for different cylinder radii for the redshift bin $1.2 < z < 1.5$. We show results only for R_2 , R_5 and R_{10} for the sake of clarity, and the reader can easily extrapolate the results for the other radii from those shown here, and from the discussion below. In Appendix C, we show the same results for the two other redshift bins.

We note that, for $\delta_N^R \rightarrow -1$, the denominator of the normalized residuals (the variable in *y*-axis in the bottom panels) approaches zero and residuals rapidly increase. This is an artefact related to our definition of residuals, as demonstrated by the upper panels in which the relation between the two density fields is well behaved close to zero.

We observe the following.

(i) our density reconstruction δ_N^E underestimates the reference density δ_N^R at the highest densities, for all cylinder radii and at all redshifts. This underestimation ranges from ~ 70 per cent for the smallest radii (R_1 and R_2) to ~ 20 per cent for the largest ones (R_8 and R_{10}).

(ii) The lowest densities are always overestimated, by a percentage that rapidly increases for $\delta_N^R \rightarrow -1$ (as explained above).

(iii) The systematic error depends on the cylinder radius (it is larger for smaller radii) at fixed redshift, and it mildly depends on

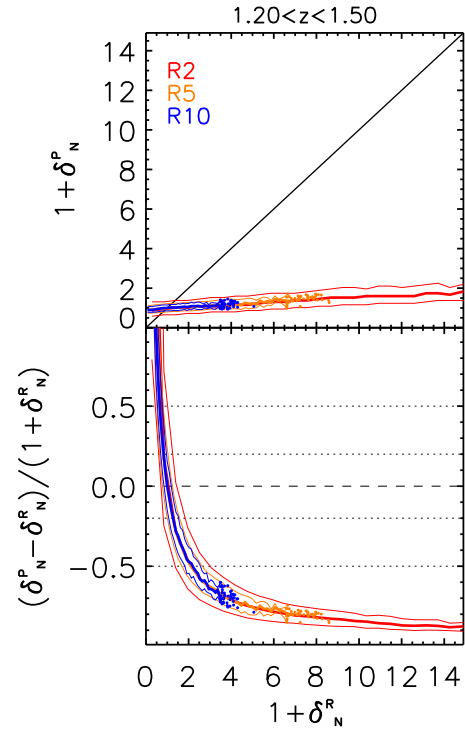


Figure 10. As in Fig. 9, but in this case we compare δ_N^R with δ_N^P .

redshift at fixed radius; this indicates that it is more difficult to reconstruct the absolute value of the local density at small scales.

(iv) The random error for the highest densities depends very mildly (if at all) on the cylinder radius (being possibly slightly larger for smaller radii) at fixed redshift, while it depends more evidently on redshift at fixed radius (it varies from $\lesssim 10$ per cent in the lowest redshift bin to ~ 10 – 15 per cent in the highest redshift bin).

(v) At the highest densities, the random error is smaller than the systematic error at all radii and redshifts, but for R_8 and for R_{10} at $z > 1.5$ where the two errors are similar.

In summary, for R_8 and R_{10} we are able to compute the absolute value of the local density field δ_N^R with a small random error and an acceptable systematic underestimate of ~ 20 per cent. For smaller scales both types of errors increase and the recovery of the density is mainly hampered by the random ones in low-density regions and by the systematic ones in the high-density peaks.

The underestimate of the highest densities in general, and especially for the smallest radii, is mainly due to the following reasons: (i) the large photometric error, that spread the ZADE weights along the line of sight on a large distance; (ii) the low density of galaxies in the DSMOCKS with respect to the density of galaxies in the DPMOCKS (see e.g. Cucciati et al. 2014, Appendix A.3, where we verified that the systematic error in the density reconstruction increases when we decrease the sampling of the spectroscopic sample); (iii) the lower clustering of the DSMOCKS with respect to the DPMOCKS (see the effects described in Appendix A).

In general, we expect to overestimate low densities and to underestimate high densities when using tracers with large redshift error, like photometric redshifts. This can be more easily seen in Fig. 10, where we compare δ_N^R and δ_N^P values on a cell-by-cell basis. The large photometric redshift error ($\sigma_{zp} = 0.05(1+z)$) displaces galaxies far away from their true distance (see the second panel

of Fig. 2), making the galaxy distribution almost homogeneous in the entire explored volume (voids are filled, and high-density regions are depopulated). As a consequence, the reconstructed density within cells is everywhere close to the cosmological mean. This produces a rather small random error, but the reconstructed δ_N^P is systematically smaller (higher) than the true one for overdense (underdense) regions, and the mismatch increases with the distance from $\delta_N^R = 0$. The same trend is found at all redshifts and for all cell sizes.

5.4 Discussion

The results shown in Sections 5.1 and 5.2 imply that using the *Euclid* Deep survey it will be possible to perform comparative studies of galaxy evolution in low- and high-density regions from large to small scales up to $z \leq 1.8$. In particular, the identification of small-scale ($R \sim 1 h^{-1}$ Mpc) high-density regions, with a very low contamination from other environments, will allow us to study the regions (like e.g. galaxy clusters and groups) where several physical processes shaping galaxy evolution normally occur. Moreover, the high completeness and very low contamination in identifying the lowest density regions on large scales ($R = 10 h^{-1}$ Mpc) indicates that one can potentially use the *Euclid* Deep survey to identify cosmic voids (see e.g. Micheletti et al. 2014 for a systematic search of cosmic voids in spheres of $R \gtrsim 15$ Mpc).

More generally, we have shown that in a sample like the *Euclid* Deep survey it will be possible to identify high densities and low densities on different scales. The potentiality of this multi-scale approach is already been demonstrated in several work in the literature. On one side, correlating galaxy properties with the local density on different scales is an effective way to understand how galaxy evolution depends on the assembly of the large-scale structure (see e.g. Wilman, Zibetti & Budavári 2010; Fossati et al. 2015 and references therein). On the other side, a multi-scale approach can also be used to identify the different components of the cosmic web (voids, filaments, walls and clusters, see e.g. Aragón-Calvo, van de Weygaert & Jones 2010; Smith et al. 2012).

Clearly, each science case will require a dedicated feasibility study. For instance, the minimum (maximum) level of completeness (contamination) required for any given science case has to be quantified case by case (see e.g. Cucciati et al. 2012b and Malavasi et al. 2016, where they study whether the contamination in the density field reconstruction hampers the detection of the colour–density relation or of the different shape of the galaxy stellar mass function in low and high densities).

The precise computation of the absolute value of the local density field is a task much more difficult than the identification of the lowest and highest densities, especially when we lack a precise measurement of the 3D position of the tracers of the density field itself. Nevertheless, our tests show that we are able to measure the value of δ_N on scales of $\geq 8 h^{-1}$ Mpc up to $z \sim 1.8$.

This achievement, for instance, will allow us to study the evolution of the galaxy bias on such scales, as compared with surveys at lower redshift (see e.g. Di Porto et al. 2014, Cappi et al. 2015, Bel et al. 2016 and references therein). Another application of a precise local density value is the detection of clusters in their phase of build-up, although by now this kind of detection has been systematically tested in the literature at higher redshifts and on slightly larger scales than those investigated here (~ 10 – $17 h^{-1}$ Mpc, $z \gtrsim 2$, see e.g. Chiang, Overzier & Gebhardt 2013, 2014).

We defer to a future work a detailed analysis of the feasibility of specific environmental studies with the *Euclid* Deep survey. As a

very simple test case, we show in Section 6 the potential ability of our method of detecting the regions where the most massive clusters lie.

6 A TEST CASE: THE RELATION BETWEEN THE LOCAL ENVIRONMENT AND GALAXY CLUSTERS

The main goal of this paper is to distinguish in a robust way the highest density peaks from the low-density regions on both small and large scales, so the precise identification of clusters, voids, and all the intermediate structures that form the cosmic web is beyond our aim. Nevertheless it is interesting to see how the density reconstructed with our mock catalogues compares with some of the typical components of the large-scale structure of the Universe. Among these components, galaxy clusters are certainly more easy to locate with a precise 3D position, rather than filaments and voids, at least in simulated DM/galaxy catalogues. Moreover, Fig. 8 shows that our identification of small-scale ($R = 1$ – $2 h^{-1}$ Mpc) high-density peaks is robust.

In Fig. 11, we show where (relatively massive) clusters are located in RA–Dec., in a small redshift bin ($1.47 < z < 1.48$) of one of our light-cones, compared to the position of galaxies in the DREF_{MOCK} and to the density fields δ_N^R and δ_N^E . The redshift bin has been chosen to be at relatively high redshift and to include at least one of the most massive clusters ($\log(M/M_\odot) > 14$), together with other overdense regions and voids.

Qualitatively, we see that clusters, and especially the most massive ones, fall in the highest density regions, and this is true for both δ_N^R and δ_N^E . In this example, the density is estimated on a scale of $R = 1 h^{-1}$ Mpc (the smallest scale we study in this work, to better compare with the typical dimension of galaxy clusters). More quantitatively, we see in Fig. 12 that the values of local density evaluated at the positions where galaxy clusters are located fall in the highest density tail of the total density distribution for both δ_N^R and δ_N^E , and there is even some correlation between the mass of the clusters and the local density value where they reside.

From Fig. 12, it is also evident that there are regions (map elements) with the same measured density as those where clusters reside, but where there are no clusters. This is both due to the contamination of our density reconstruction and to the fact that our method is not fine-tuned to identify clusters as the highest density peaks. Nevertheless this simple sanity check shows the potentiality of future galaxy surveys in the study of the large-scale structure of the Universe.

7 SUMMARY AND CONCLUSIONS

We studied the feasibility of environmental studies in slitless spectroscopic surveys from space. In particular, we want to exploit the synergy between spectroscopic and photometric samples. As a test case, we use galaxy mock catalogues which mimic the future *Euclid* Deep surveys, namely a spectroscopic survey limited in $H\alpha$ flux and a photometric survey limited in H band. Our main goal is to verify that it will be possible to disentangle the highest from the lowest density regions, by means of the parametrization of the local environment. We anchored the photometric redshifts of the photometric sample to the 3D skeleton of the spectroscopic sample, and we measured the local environment on different scales, from 1 to $10 h^{-1}$ Mpc, in different redshift bins in the range $0.9 < z < 1.8$. We found that:

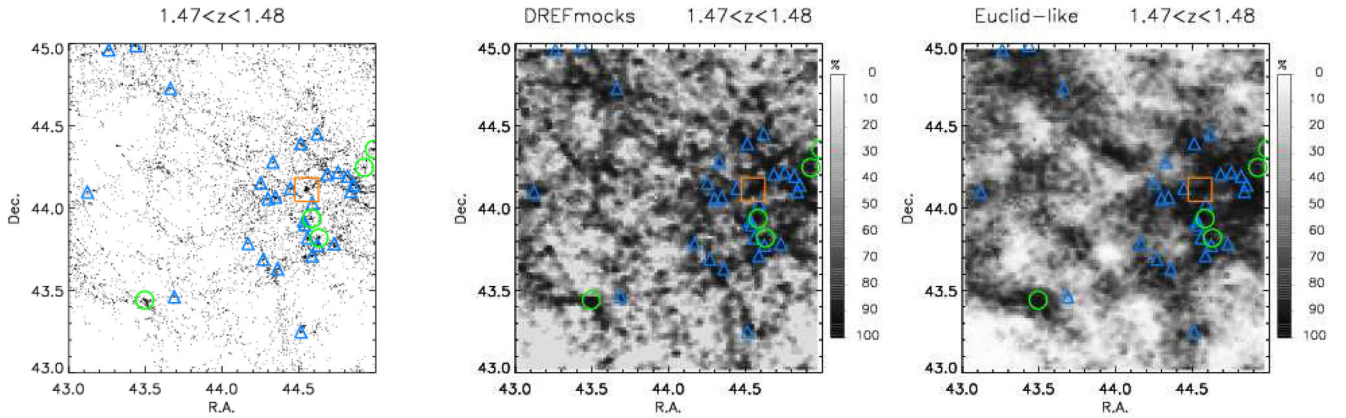


Figure 11. Left. RA–Dec. distribution of galaxies in one of the DREFMOCKS, for the redshift bin $1.47 < z < 1.48$. Blue triangles, green circles and orange squares locate the position of galaxy clusters (in this same redshift bin) with total masses of $\log(M/M_{\odot}) \in [13, 13.5)$, $[13.5, 14)$, and > 14 , respectively. Middle. In the same RA, Dec. and redshift range as in the left-hand panel, the grey-scale colour map represents the density field estimated in the DREFMOCK with cylinders of $R = 1 h^{-1} \text{Mpc}$ per element. The density value in each grid element is computed averaging the δ_N^R values of the cylinders falling in that given grid element. The grey-scale refers to the percentiles of the δ_N^R distribution as in the colour bar. Triangles, circles and squares are as in the left-hand panel. Right. As in the middle panel, but here we use δ_N^E instead of δ_N^R .

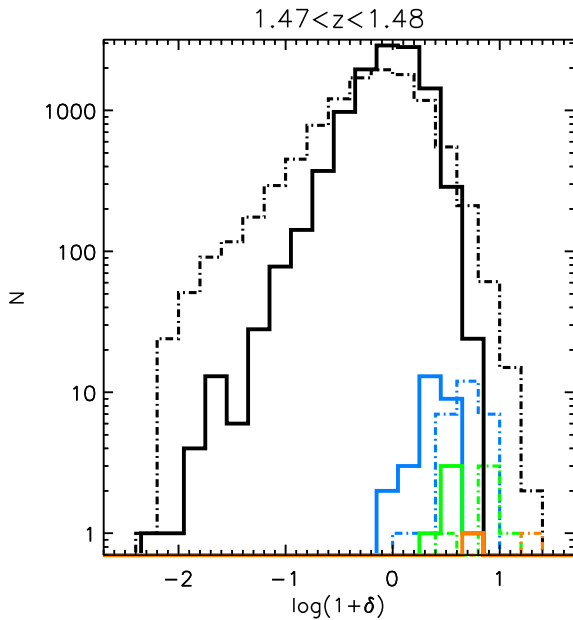


Figure 12. Distribution of densities from the density maps presented in Fig. 11: the black dot–dashed histogram is for the DREFMOCK (δ_N^R) and the black solid histogram is for the DPMOCK+DSMOCK (δ_N^E). Blue, green and orange histograms represent the density distribution of the map elements of Fig. 11 where the three classes of galaxy clusters fall (see the caption of Fig. 11 for the definition of the three classes, here we use the same colour code). Also for the clusters, the dot–dashed histograms refer to δ_N^R and the solid histograms to δ_N^E .

(i) we are able to disentangle the highest densities from the lowest densities at all explored redshifts, and for all radii.

(ii) For R_8 and R_{10} at all redshifts, and for R_5 at $0.9 < z < 1.2$, it is also possible to select an intermediate-density regime, robustly separated from the highest and lowest density tails.

(iii) When we select the tail of highest densities, the contamination from poorly measured low densities decreases for larger radii and at lower redshift, while the completeness increases. Completeness is $\gtrsim 60$ per cent if we select the tails of the highest 20 per cent

using R_1 . This percentage becomes 70 and 80 per cent for R_3 and R_8 , respectively. The contamination is always $\lesssim 1$ per cent, at all redshifts and for all radii, with the exception of R_1 for which it reaches a few per cent at the highest redshift.

(iv) When we move to the more demanding task of computing the precise density values, our density reconstruction underpredicts galaxy counts in the highest densities, for all cylinder radii and at all redshifts, by a factor ranging from ~ 70 per cent for the smallest radii (R_1 and R_2) to ~ 20 per cent for the largest ones (R_8 and R_{10}). Moreover, the error budget at low density is dominated by the random error, while at the highest densities it is dominated by the systematic error. This is true for all radii, with the exception of R_8 and R_{10} at high density, where the random and systematic error are comparable.

(v) As a qualitative test case, we verified that in a given redshift bin at $z \sim 1.5$, chosen to include at least a small sample of relatively high-mass galaxy clusters ($\log(M/M_{\odot}) > 13.5$), the galaxy clusters reside in the highest tail of the density distribution, when the density is estimated on a scale of $R = 1 h^{-1} \text{Mpc}$.

Our results show that environmental studies can be efficiently performed in photometric samples if spectroscopic information is available for a smaller sample of objects that sparsely samples the same volume. Namely, we are able to robustly identify the highest density peaks from the lowest density regions using slitless spectroscopy coupled with a deep photometric sample, like in the *Euclid* Deep survey.

In particular, the redshift range probed by this survey ($0.7 \lesssim z \lesssim 2$) covers the epoch when the relation between local environment and galaxy properties has been observed to change with respect to the local Universe (Cucciati et al. 2006; Lin et al. 2016 at $z \gtrsim 1.2$, Elbaz et al. 2007 at $z \gtrsim 1$). Provided that the spectroscopic redshift information is crucial to study small-scale environment, only relatively small ground-based spectroscopic surveys have been able so far to study galaxy evolution at $z > 1$ (e.g. VVDS and DEEP2), while the largest ones are too shallow (see e.g. zCOSMOS and VIPERS) to probe these epochs. The possibility to verify these earlier findings at $z > 1$ with more statistics and on smaller scales will be one of the most important scientific results from the ancillary science foreseen for the *Euclid* survey.

ACKNOWLEDGEMENTS

OC and AC acknowledge the support from grants ASI-INAF I/023/12/0 ‘Attività relative alla fase B2/C per la missione *Euclid*’ and MIUR PRIN 2010-2011 ‘The dark Universe and the cosmic evolution of baryons: from current surveys to *Euclid*’. OC acknowledges the support from grant PRIN INAF 2014 ‘VIPERS: unveiling the combined evolution of galaxies and large-scale structure at $0.5 < z < 1.2$ ’. OC thanks Sandro Bardelli, Fabio Bellagamba, Lauro Moscardini and Mauro Roncarelli, for useful discussions. The Millennium Simulation data bases used in this paper and the web application providing online access to them were constructed as part of the activities of the German Astrophysical Virtual Observatory.

REFERENCES

- Adami C. et al., 2010, *A&A*, 509, A81
Aragón-Calvo M. A., van de Weygaert R., Jones B. J. T., 2010, *MNRAS*, 408, 2163
Atek H. et al., 2010, *ApJ*, 723, 104
Atek H. et al., 2011, *ApJ*, 743, 121
Bel J. et al., 2016, *A&A*, 588, A51
Bellagamba F., Maturi M., Hamana T., Meneghetti M., Miyazaki S., Moscardini L., 2011, *MNRAS*, 413, 1145
Bielby R. et al., 2012, *A&A*, 545, A23
Bolzonella M. et al., 2010, *A&A*, 524, A76
Cappi A. et al., 2015, *A&A*, 579, A70
Cassata P. et al., 2007, *ApJS*, 172, 270
Chen H.-W. et al., 2002, *ApJ*, 570, 54
Chiang Y.-K., Overzier R., Gebhardt K., 2013, *ApJ*, 779, 127
Chiang Y.-K., Overzier R., Gebhardt K., 2014, *ApJ*, 782, L3
Christodoulou L. et al., 2012, *MNRAS*, 425, 1527
Coil A. L. et al., 2008, *ApJ*, 672, 153
Cooper M. C., Newman J. A., Madgwick D. S., Gerke B. F., Yan R., Davis M., 2005, *ApJ*, 634, 833
Cristóbal-Hornillos D. et al., 2009, *ApJ*, 696, 1554
Cucciati O. et al., 2006, *A&A*, 458, 39
Cucciati O. et al., 2010, *A&A*, 524, A2
Cucciati O. et al., 2012a, *A&A*, 539, A31
Cucciati O. et al., 2012b, *A&A*, 548, A108
Cucciati O. et al., 2014, *A&A*, 565, A67
Darvish B., Mobasher B., Sobral D., Scoville N., Aragon-Calvo M., 2015, *ApJ*, 805, 121
Davidzon I. et al., 2016, *A&A*, 586, A23
Di Porto C. et al., 2014, preprint ([arXiv:1406.6692](https://arxiv.org/abs/1406.6692))
Dressler A. et al., 2012, preprint ([arXiv:1210.7809](https://arxiv.org/abs/1210.7809))
Elbaz D. et al., 2007, *A&A*, 468, 33
Fossati M. et al., 2015, *MNRAS*, 446, 2582
Frith W. J., Metcalfe N., Shanks T., 2006, *MNRAS*, 371, 1601
Garilli B. et al., 2014, *A&A*, 562, A23
Geach J. E., Smail I., Best P. N., Kurk J., Casali M., Ivison R. J., Coppin K., 2008, *MNRAS*, 388, 1473
Geach J. E. et al., 2010, *MNRAS*, 402, 1330
Geach J. E., Sobral D., Hickox R. C., Wake D. A., Smail I., Best P. N., Baugh C. M., Stott J. P., 2012, *MNRAS*, 426, 679
Gonzalez-Perez V., Lacey C. G., Baugh C. M., Lagos C. D. P., Helly J., Campbell D. J. R., Mitchell P. D., 2014, *MNRAS*, 439, 264
Green J. et al., 2012, preprint ([arXiv:1208.4012](https://arxiv.org/abs/1208.4012))
Gunn J. E., Gott J. R. I., 1972, *ApJ*, 176, 1
Guzzo L. et al., 2007, *ApJS*, 172, 254
Guzzo L. et al., 2014, *A&A*, 566, A108
Ilbert O. et al., 2013, *A&A*, 556, A55
Ilbert O. et al., 2015, *A&A*, 579, A2
Jeon Y., Im M., Kang E., Lee H. M., Matsuhara H., 2014, *ApJS*, 214, 20
Jian H.-Y. et al., 2014, *ApJ*, 788, 109
Kodama T., Tanaka I., Kajisawa M., Kurk J., Venemans B., De Breuck C., Vernet J., Lidman C., 2007, *MNRAS*, 377, 1717
Komatsu E. et al., 2011, *ApJS*, 192, 18
Kovač K. et al., 2010, *ApJ*, 708, 505
Lagos C. D. P., Bayet E., Baugh C. M., Lacey C. G., Bell T. A., Fanidakis N., Geach J. E., 2012, *MNRAS*, 426, 2142
Lai C.-C. et al., 2016, *ApJ*, 825, 40
Larson R. B., Tinsley B. M., Caldwell C. N., 1980, *ApJ*, 237, 692
Laureijs R. et al., 2011, preprint ([arXiv:1110.3193](https://arxiv.org/abs/1110.3193))
Lemson G., Virgo Consortium t., 2006, preprint ([astro-ph/0608019](https://arxiv.org/abs/astro-ph/0608019))
Li C., Kauffmann G., Jing Y. P., White S. D. M., Börner G., Cheng F. Z., 2006, *MNRAS*, 368, 21
Lilly S. J. et al., 2007, *ApJS*, 172, 70
Lin L. et al., 2016, *ApJ*, 817, 97
Ly C., Lee J. C., Dale D. A., Momcheva I., Salim S., Staudaher S., Moore C. A., Finn R., 2011, *ApJ*, 726, 109
McCarthy P. J. et al., 1999, *ApJ*, 520, 548
McNaught-Roberts T. et al., 2014, *MNRAS*, 445, 2125
Madau P., Dickinson M., 2014, *ARA&A*, 52, 415
Malavasi N., Pozzetti L., Cucciati O., Bardelli S., Cimatti A., 2016, *A&A*, 585, A116
Marulli F. et al., 2013, *A&A*, 557, A17
Marulli F., Veropalumbo A., Moresco M., 2016, *Astron. Comput.*, 14, 35
Mazure A. et al., 2007, *A&A*, 467, 49
Meneux B. et al., 2008, *A&A*, 478, 299
Merson A. I. et al., 2013, *MNRAS*, 429, 556
Metcalfe N., Shanks T., Weibacher P. M., McCracken H. J., Fong R., Thompson D., 2006, *MNRAS*, 370, 1257
Micheletti D. et al., 2014, *A&A*, 570, A106
Moore B., Katz N., Lake G., Dressler A., Oemler A., 1996, *Nature*, 379, 613
Moy E., Barmby P., Rigopoulou D., Huang J.-S., Willner S. P., Fazio G. G., 2003, *A&A*, 403, 493
Oke J. B., 1974, *ApJS*, 27, 21
Peng Y.-j. et al., 2010, *ApJ*, 721, 193
Pozzetti L. et al., 2016, *A&A*, 590, A3
Retzlaff J., Rosati P., Dickinson M., Vandame B., Rit e C., Nonino M., Censky C., GOODS Team, 2010, *A&A*, 511, A50
Scoville N. et al., 2007, *ApJS*, 172, 150
Scoville N. et al., 2013, *ApJS*, 206, 3
Shim H., Colbert J., Teplitz H., Henry A., Malkan M., McCarthy P., Yan L., 2009, *ApJ*, 696, 785
Smith A. G., Hopkins A. M., Hunstead R. W., Pimblet K. A., 2012, *MNRAS*, 422, 25
Spitler L. R. et al., 2012, *ApJ*, 748, L21
Springel V. et al., 2005, *Nature*, 435, 629
Teplitz H. I., Gardner J. P., Malumuth E. M., Heap S. R., 1998, *ApJ*, 507, L17
Thompson R. I., Storrie-Lombardi L. J., Weymann R. J., Rieke M. J., Schneider G., Stobie E., Lytle D., 1999, *AJ*, 117, 17
Toomre A., Toomre J., 1972, *ApJ*, 178, 623
Wilman D. J., Zibetti S., Budav ari T., 2010, *MNRAS*, 406, 1701
Yan L., McCarthy P. J., Freudling W., Teplitz H. I., Malumuth E. M., Weymann R. J., Malkan M. A., 1999, *ApJ*, 519, L47

APPENDIX A: THE EFFECTS OF THE DIFFERENT SELECTION FUNCTION OF THE PHOTOMETRIC AND SPECTROSCOPIC CATALOGUES

The strength of the ZADE method resides in the fact that the spectroscopic sample, when it is a random subsample of the photometric one, has the same clustering properties as the photometric sample, and so it is the perfect data set to anchor the z_p . In the case of *Euclid*, the spectroscopic and photometric samples are selected with two different selection functions, and so they are not supposed to have the same clustering properties. This is shown in Fig. 4, where we plot the value of $\xi(s)$ for the *Euclid* spectroscopic and photometric samples.

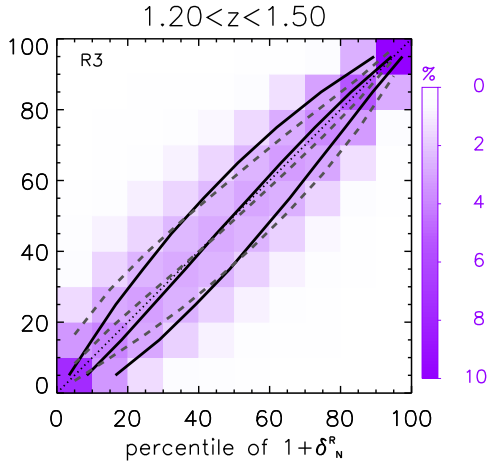


Figure A1. As in the top-right panel of Fig. 6, but in this case the spectroscopic catalogue used for ZADE is a random subsample of the photometric catalogue.

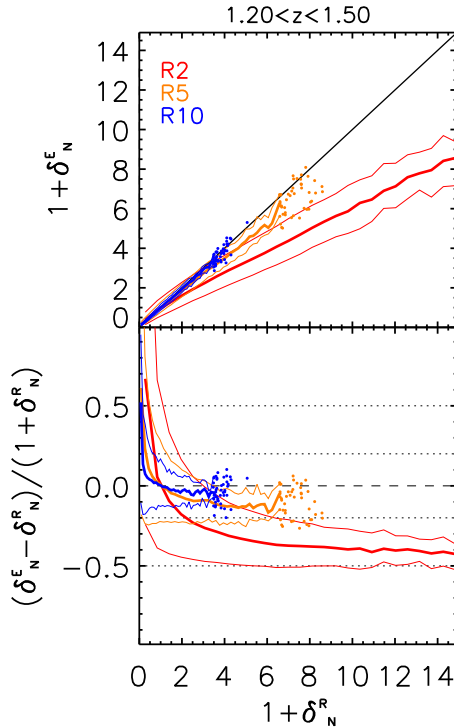


Figure A2. As in Fig. 9, but in this case the spectroscopic catalogue used for ZADE is a random subsample of the photometric catalogue.

In this appendix, we show which are the differences, in the density field reconstruction, when we use a spectroscopic sample like the one expected in *Euclid* and another one that is a random subsample of the photometric one (but with same number of galaxies as in the DS_{MOCKS}).

We extracted from the DREF_{MOCKS} a random galaxy subsample with the same redshift distribution $n(z)$ as the DS_{MOCKS}. In these new catalogues, the redshift of the galaxies mimics the *Euclid* spectroscopic redshift, i.e. it corresponds to the cosmological redshift, plus the peculiar velocity, plus the spectroscopic measurement error as in the DS_{MOCKS}. We applied again ZADE on the DP_{MOCK} catalogues, but using these new catalogues as spectroscopic skeleton, and then we estimated δ_N using the new ZADE output.

Fig. A1 shows the joint probability (only for R_3) and Fig. A2 the cell-by-cell comparison. Fig. A2 shows that if we use these new spectroscopic catalogues we obtain a better reconstruction of the density field for the overdense regions, namely obtaining a much smaller systematic error (with respect to Fig. 9). The results for the other radii and redshift bins are very similar. In particular, for $R > 5 h^{-1} \text{Mpc}$ the systematic error in the density reconstruction is very close to zero for the overdense regions when using these new spectroscopic catalogues.

APPENDIX B: THE EFFECTS OF THE VARIATION OF THE FLUX LIMIT OF THE SPECTROSCOPIC SURVEY

In this appendix, we show how our results would change if we used a more conservative flux cut in our DS_{MOCKS}, i.e. $10^{-16} \text{ erg cm}^{-2} \text{ s}^{-1}$

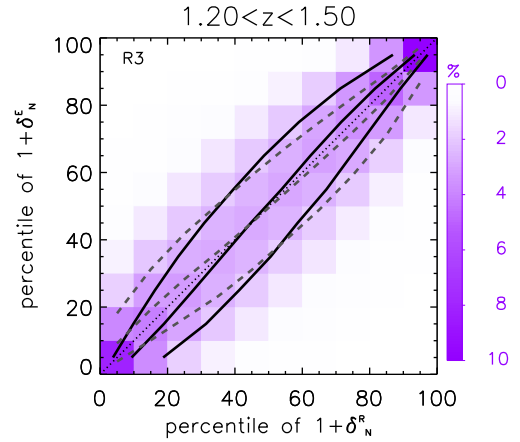


Figure B1. As the top-right panel of Fig. 6, but in this case the DS_{MOCKS} have an $H\alpha$ flux limit of $10^{-16} \text{ erg cm}^{-2} \text{ s}^{-1}$.

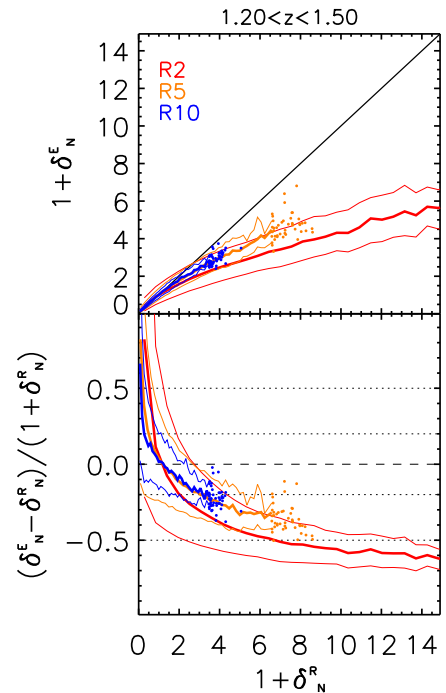


Figure B2. As in Fig. 9, but in this case the DS_{MOCKS} have an $H\alpha$ flux limit of $10^{-16} \text{ erg cm}^{-2} \text{ s}^{-1}$.

$\text{cm}^{-2} \text{s}^{-1}$ instead of $7 \times 10^{-17} \text{ erg cm}^{-2} \text{ s}^{-1}$ (Figs B1 and B2). This brighter cut corresponds to the flux limit of the Deep survey at $\sim 7\sigma$. To create these brighter DS_{MOCKS} we used the same procedure as for our original DS_{MOCKS}, including the mimicking of 2 per cent of purity and completeness.

Comparing the results in Fig. B2 with those in Fig. 9, we can see that the density field reconstruction is only slightly hampered by the use of the brighter cut. Namely, the brighter cut causes a slightly larger random error in the density reconstruction, while the systematic error remains similar. This result holds at all explored redshifts, and also for the other cylinder radii not showed in Fig. B2.

APPENDIX C: DENSITY FIELD RECONSTRUCTION IN OTHER REDSHIFT BINS

We show here our results on the density field reconstruction in the redshift ranges $0.9 < z < 1.2$ and $1.5 < z < 1.8$ when using our original DS_{MOCKS}. Figs C1 and C2 are the same as Fig. 6, and Fig. C3 is the same as Fig. 9, but for these different redshift ranges. Results are discussed in Sections 5.1 and 5.3, respectively.

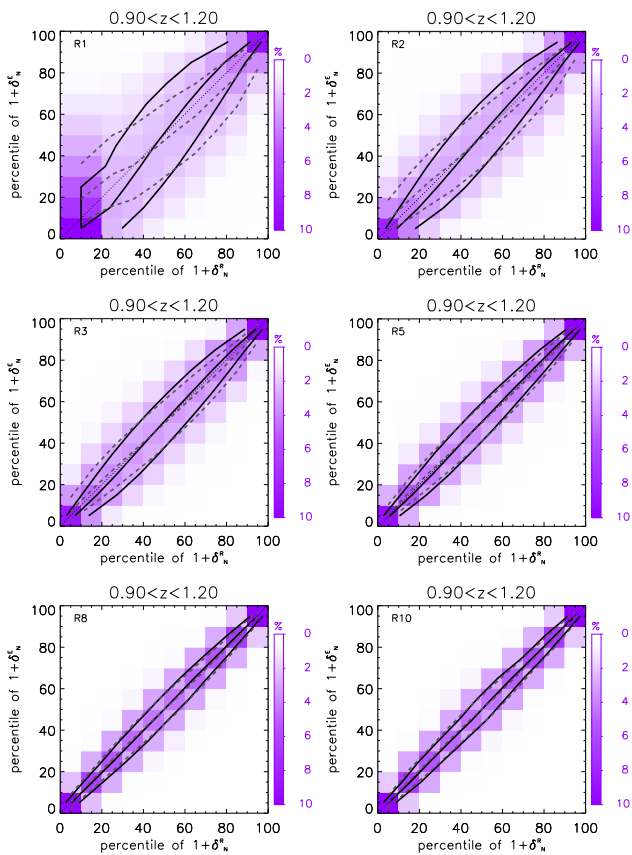


Figure C1. As in Fig. 6, but for the redshift range $0.9 < z < 1.2$.

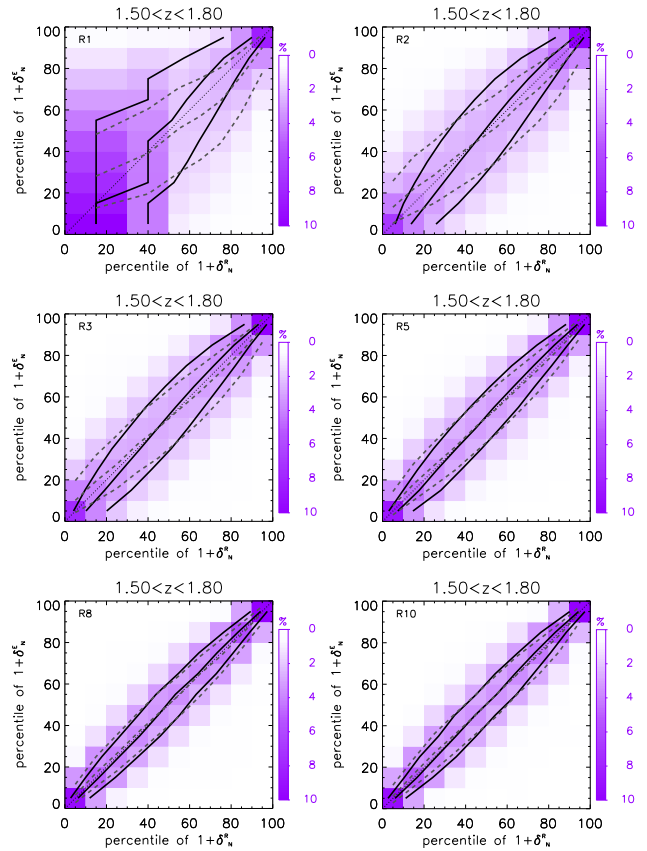


Figure C2. As in Fig. 6, but for the redshift range $1.5 < z < 1.8$.

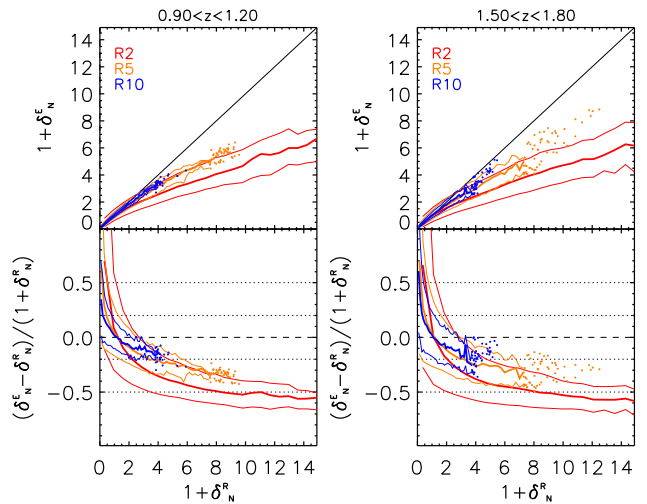


Figure C3. As in Fig. 9, but for the redshift bins $0.9 < z < 1.2$ (left) and $1.5 < z < 1.8$ (right).

This paper has been typeset from a \LaTeX file prepared by the author.